THESIS FOR DEGREE OF LICENTIATE OF ENGINEERING

Multiscale Modeling of Interfaces

SVEN JOHANSSON

Department of Applied Physics
CHALMERS UNIVERSITY OF TECHNOLOGY
Göteborg, Sweden 2007

Multiscale Modeling of Interfaces
SVEN JOHANSSON

Department of Applied Physics
Chalmers University of Technology
SE-412 96 Göteborg, Sweden
Sweden
Telephone +46–(0)31–7721000

Chalmers reproservice
Göteborg, Sweden 2007

Multiscale Modeling of Interfaces
SVEN JOHANSSON
Department of Applied Physics
Chalmers University of Technology

ABSTRACT

Understanding strength and stability of interfaces between dissimilar materials or phases is a highly active field of contemporary materials research. Knowledge of interface structure and energetics is important for modeling of complex materials both on a mechanical and thermodynamical level as well as for many functional properties. Interfaces is a collective term including surfaces, interphase boundaries and grain boundaries. A general interface can be sharp or diffuse, planar or corrugated. The interface between two crystals is usually quite sharp, and can be classified as coherent, semicoherent or incoherent depending on the mismatch between the adjoining crystals.

The goal of this Thesis is to obtain a better understanding of interfacial structures and energetics, in particular of semicoherent interfaces. Previous first-principles work in the field has often excluded the effect of misfit. Therefore, we present a simple model combining the interfacial interaction from first-principles methods with a continuum description to account for the elastic displacements. The accuracy of the model has been satisfactorily tested against atomistic modelling.

We investigate the effect of misfit on interfaces in two classes of materials: steels and cemented carbides. In the first case, we study the interface between Fe and a VN precipitate. The results show that even a small misfit (2 %) has a large influence on the interface energy. In the second case, we apply the method to the semicoherent $\Sigma = 2$ twist boundary found in both tungsten carbide powder and sintered cemented carbides. The results are discussed in the context of grain boundary evolution during sintering.

Keywords: interfaces, misfit, first-principles calculations, density-functional theory, DFT, cemented carbides, WC-Co, hard metals, grain boundaries, microstructure, VN precipitates, semicoherent interfaces, Peierls-Nabarro model.

LIST OF PUBLICATIONS

This thesis consists of an introductory text and the following papers:

I **Interface Energy of Semicoherent Metal-Ceramic Interfaces**
S. A. E. Johansson, M. Christensen, and G. Wahnström
Physical Review Letters **95**, 226108 (2005).

II **An *ab initio* based approach for interface energy calculations of semicoherent metal-ceramic interfaces**
S. A. E. Johansson, M. Christensen, and G. Wahnström
(in manuscript)

Contents

CHAPTER 1

Introduction

Materials properties depend on phenomena on several different length scales from Ångströms, where the electronic bonds gluing the atoms into solids are the important constituents, up to millimeters, where the microstructure with its different phases and boundaries is the subject of study. Eventually, at the macroscopic level, the finer scales are merged into a continuum description. Navigating through these scales and understanding how atomic structure relates to the final properties of the material poses a true challenge for the modern materials scientist. It is not clear how macroscopically measurable quantities, such as hardness, strength and ductility, connect to total energy and electronic structure.

The subject of this Thesis is interfaces which belongs to a group of structures of length scale one step above the single atom. Understanding strength and stability of interfaces between dissimilar materials or phases is a highly active field of contemporary materials research. Knowledge of interface structure and energetics is important for modeling of complex materials both on a mechanical and thermodynamical level as well as for many functional properties. Interfaces is a collective term including surfaces, interphase boundaries and grain boundaries. A general interface can be sharp or diffuse, planar or corrugated. The interface between two crystals is usually quite sharp, and can be classified as coherent, semicoherent or incoherent depending on the mismatch between the adjoining crystals.

In this Thesis, we have modeled interfaces using first-principles methods. Due to their predictive power, first-principles calculations are extra valuable as it comes to determining interfacial properties, since these are utterly difficult to determine experimentally. E. g. measurements of interface energies often come from wetting experiments, which has limited bearing to solid-solid interfaces. Moreover, modeling of interfaces is also a difficult task due to the restrictions of system size imposed by the available computational power. In most first-principles modeling, the interface is assumed to be sharp, planar and coherent, although the latter assumption is nearly always violated for real interfaces. In addition, temperature-dependent effects are often neglected. Today, only vibrational degrees of freedom in a solid can be rigourously included in a first-principles calculation, and pronounced entropic systems, such as the solid-liquid interface, are still waiting for a first-principles treatment.

The semicoherent interface between crystals adds a bit of extra complexity compared to the coherent interface. Due to its well-defined structure of misfit dislocations, it is in reach of first-principles methods. However, the required system size is currently beyond our computational capacity. In this Thesis, we present a method of combining first-principles calculations in the framework of density functional theory (DFT) with elasticity theory to assess the effect of misfit on interfacial structure and energetics. The idea originates from the Peierls-Nabarro model of dislocations, and is here applied to two cases: the interphase Fe/VN interface, and, in some detail, the special $\Sigma = 2$ twist grain boundary in WC.

The technique of combining different scales in modeling is called multiscale modeling and explains the title of the present Thesis. The passing of information across scales – from the atomistic to the continuum level – is often denoted sequential multiscale modeling in contrast to concurrent multiscale modeling techniques, where the scales are coupled seamlessly.

The following sections of Chapter 1 provide a brief background to the materials under study, namely steels and cemented carbides. In Chapter 2, some basics of the continuum description of materials are presented. Chapter 3 deals with the atomistic description of materials, from first-principles density functional theory to model potentials. In Chapter 4, a method for determining energies of semicoherent interfaces is developed and applied. Chapter 5 summarizes and concludes the work performed and also contains some proposals of future work on interface modeling.

1.1 Steels

Steels represent not only the most widely used metallic materials, but also perhaps the most complex group of alloys. Despite the mechanical weakness of pure iron, steels show a diversity in mechanical properties with yield stresses spanning from 200 MPa to 5500 MPa [1]. The common denominator among steels is the addition of carbon to iron. Such low concentrations of carbon as 0.5 atomic percent have a decisive strengthening effect on iron.

As suggested in the 1930s by Taylor, Orowan, and Polanyi, plastic deformation in many crystals occurs by slip mediated by the movement of dislocations. Compared to Fe atoms, C atoms have such small atomic size that they usually become interstitial solute atoms of high diffusivity. Due to the mismatch in size with the surrounding matrix, the solute atoms will give rise to an elastic field and are likely to be found in the vicinity of dislocations, where the distorted lattice provides room for favorable interstitial sites. Effectively, the C atoms acts as hinders for the dislocation movement thus increasing the strength of the metal.

Several other important strengthening methods exist. Grain boundaries limit the mean free path for the dislocation making a fine-grained material more likely to resist plastic deformation. One must however keep in mind, that, at least for incoherent boundaries, the resistance towards grain boundary sliding is low and this mode of plastic deformation may dominate a fine-grained material. During work hardening, the metal undergoes mechanical work of high enough frequency and magnitude to not only move dislocations, but also to create new ones. The created dislocations entangle and lock each other. Too aggressive hardening will, however, make the material brittle, since the lack of mobile dislocations will instead induce the formation of cracks when the material is put under tension.

A phase-diagram of the Fe-C system is given in Figure 1.1. In the low temperature regime, the magnetic α-phase of bcc structure also known as ferrite is stable. For pure Fe, a phase transformation to the non-magnetic γ-phase known as austenite takes place at $912\,^\circ$C, but the temperature of transformation drops rapidly with carbon content and has stabilized at $723\,^\circ$C already at 0.1 weight% C. Addition of carbon will cause iron carbides (Fe_3C known as cementite) to form existing in equilibrium with the α- and γ-phases. An effect of adding metallic alloying elements is to change the size and shape of the γ-field region of the phase diagram and support the formation of either austenite or ferrite. As an example, Ni is an austenite former used in stainless steels [1]. For applications in environments of high stress levels, α-Fe is preferred, whose formation is promoted by e. g. Nb and V.

The strengthening mechanism of interest in this work is precipitation formation. The first step of the strengthening is to form a solid solution of carbon, nitrogen, and other metallic alloying elements. Cooling will lead to a supersaturation of the solid solution and during a subsequent application of an appropriate heat treatment, excess solutes will precipitate to form a second phase. Examples of precipitates are $M_{23}C_6$, MX, and M_2X, where M is a metal atom and X is C or N [1]. In the appended papers, examples of the nacl MN (VN, TiN, ScN) phase are studied.

The role of the precipitates is to act as obstacles for gliding dislocations. If a dislocation moving along its glide plane encounters a precipitate, it can proceed by cutting through the particle or avoid it by bowing out around the particle, eventually leaving a dislocation loop around the precipitate [2]. At higher temperatures, it is possible for the dislocation to climb and continue gliding past the precipitate. These obstacle avoiding processes all require energy and therefore enhances the strength of the material.

The formation of precipitates is directly dependent on the interface energy between the precipitate and the matrix, since it governs the rate of nucleation and growth. Hence an understanding of these processes is essential to be able to predict long-term structural changes in steel, or, more specifically, its creep resistance, i. e. its ability to withstand stress applied during a long time period.

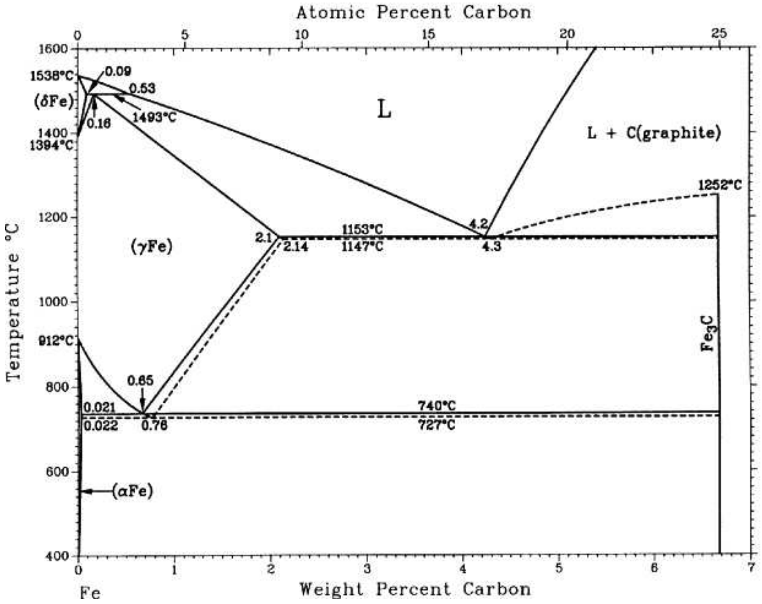

Figure 1.1: A phase diagram of the Fe-C system from [3].

1.2 Cemented carbides

By its unique combination of hardness and toughness, the class of materials known as cemented carbides has been a true success ever since its conception in the 1920s. Today, the material has found its way into a diversity of applications ranging from tire studs over tomato crushing to rock drilling. A comparison of hardness and toughness for different classes of materials is given in Figure 1.2.

The history of cemented carbides began in the end of the 19th century, when the French scientist Henri Moissan synthesized and characterized hard compounds formed by transition metals in combination with boron, carbon, and nitrogen. Around 1920, the German scientists in the Osram Studiengesellschaft were given the task of finding replacements for diamond in the drawing dies used in tungsten filament production. Earlier attempts by German scientists of utilizing Moissan's findings had given a coarse-grained material that, indeed, was very hard but also brittle. The Osram team had long experience of tungsten metallurgy due to its applications in the electrical industry, and found a way of synthesizing tungsten and carbide powder into a fine-grained tungsten carbide. However, it was not until the addition of a metal from the iron group that the group made its important break-through. Eventually, cobalt turned out to be the best additive. Originally, the material was called 'Hartmetall', but the term has been replaced by its American counterpart, 'cemented carbides', where the latter name regards the carbide grains as cemented in the cobalt binder phase.

From the first attempts of the Osram team, the properties of cemented carbides developed steadily in the forthcoming decades by the introduction of other carbide formers such as Ti, Ta, and Nb, and grain growth inhibitors such as Cr and V. A

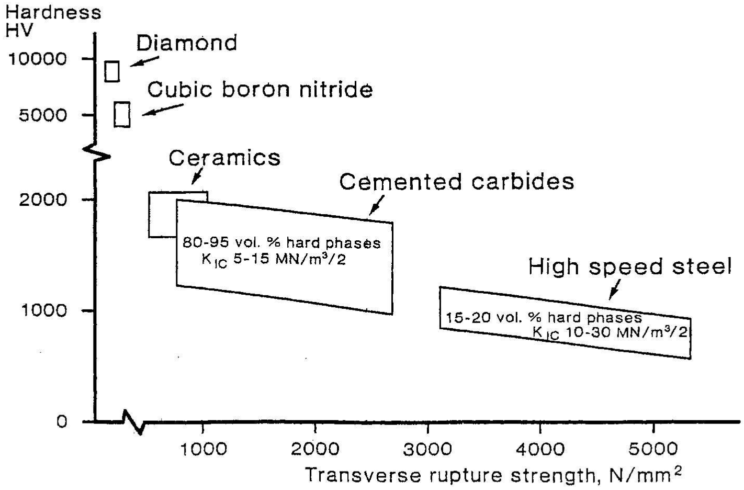

Figure 1.2: A comparison of hardness and toughness for different classes of materials from [4].

major leap in development was taken with the introduction of alumina coatings in the late 1960s. An excellent account of the history of cemented carbides is given in [4].

1.2.1 Manufacturing

Production of cemented carbides is done through means of powder metallurgy. The brittleness and high melting temperature of WC (well above 3000 K) excludes conventional metallurgical methods such as casting. Instead the method of sintering is used, where the material is heated to a temperature below the melting temperature of the carbides, but above the melting temperature of the binder, until the carbide grains adhere to each other.

Today, powders of carbides and binder are commercially available products, whose manufacture, although interesting from a chemical perspective, will not be considered here. The first step of the cemented carbide production is milling the powder to obtain a homogeneous mixture and the desired average carbide grain size. Both alcohol, used as a milling liquid, and a wax providing firmness to the unsintered product, are added during this stage. After drying the milled powders from the alcohol, the agglomerated powder (the so called green body) is pressed, usually uniaxially, to the desired shape. The shape will be approximately retained throughout the sintering, while the linear shrinkage will be $17-25\,\%$ [5].

The objective of the sintering is to strengthen the material by reducing the number of pores and creating strong intergrain adhesion. In practice, this is accomplished by inserting the green body into a heat furnace of well-controlled temperature and atmosphere. The heat treatment is performed in several steps [6]. During the first step, the temperature is ramped up to around $400\,^\circ$C, which eliminates the wax added at the milling stage. From this level, the temperature is gradually increased to the final sintering temperature of around 1400 ° C with some holds along the way to permit outgassing of oxides originating from oxygen residing on the powder surfaces. The melting of the binder at around 1300 ° C divides the sintering into solid-state sintering and liquid-phase sintering.

The driving force in the sintering process is the reduction of surface and interface energies. Already in the solid-state sintering there is a significant diffusion of especially carbon atoms into the binder. Further elevated temperatures increase both diffusivity and solubility of carbon and tungsten in the binder. The liquid-phase sintering is divided into three stages: Rearrangement, solution reprecipitation, and coarsening.

In the rearrangement process, densification occurs when the carbide grains contract due to capillarity from the penetrating binder phase spreading along the WC surfaces. For fine-grained materials, this process starts already during solid-state sintering. The liquid phase will dissolve surface layers of the carbide grains and separate polycrystalline carbide particles by penetrating the grain boundaries. Since small grains have large surface energy, they will dissolve into the melt and tungsten and carbon will reprecipitate in equal amounts on the larger grains. This step yields a change in morphology, since reprecipitation preferably occurs on low-energetic interfaces making the grains more prismatic. The time and temperature of sintering are important process parameters. On one hand, full densification and uniformity of the material is desired, but on the other hand, grain coarsening leads to embrittlement.

The carbon activity is a critical parameter, which needs to be carefully tuned in order to reach the desired window of the phase diagram as seen in Figure 1.3. Lack of carbon induces the formation of η-phase M_6C, whereas a surplus yields graphite precipitates. Both act strongly deteriorating on materials properties. Guidance to a correct initial composition is today accurately provided by mathematical models of phase equilibria and thermodynamical databases, as implemented in the Thermocalc program [7]. However, carbon activity is affected by traces of oxygen in the powder and the atmosphere of the furnace. Maintaining the correct activity is therefore a matter of experience.

1.2.2 Microstructure

A typical microstructure of the sintered WC-Co system is depicted in Figure 1.4. As the name suggests, the hard carbide grains are cemented in the tough binder. A tendency for the grains to be of truncated triangular shape is seen – as typical for WC grains sintered in Co [9]. The material in the image has the composition Co 9.89 wt%, C 5.41 wt% and W 84.70 wt% and an average grain size of $0.708\,\mu$m [10]. The average grain size is here taken as the equivalent circle diameter, which is linearly related to the actually measured grain size in the image.

WC has a hexagonal structure of space group $P\bar{6}m2$ of lattice parameters $a = 2.906$ Å and $c = 2.837$ Å [5]. Two sets of planes are of special interest. These are the basal planes $\{0001\}$ and the prismatic planes $\{10\bar{1}0\}$. Due to the geometry, the surfaces of the prismatic planes come in two non-equivalent versions depending on the

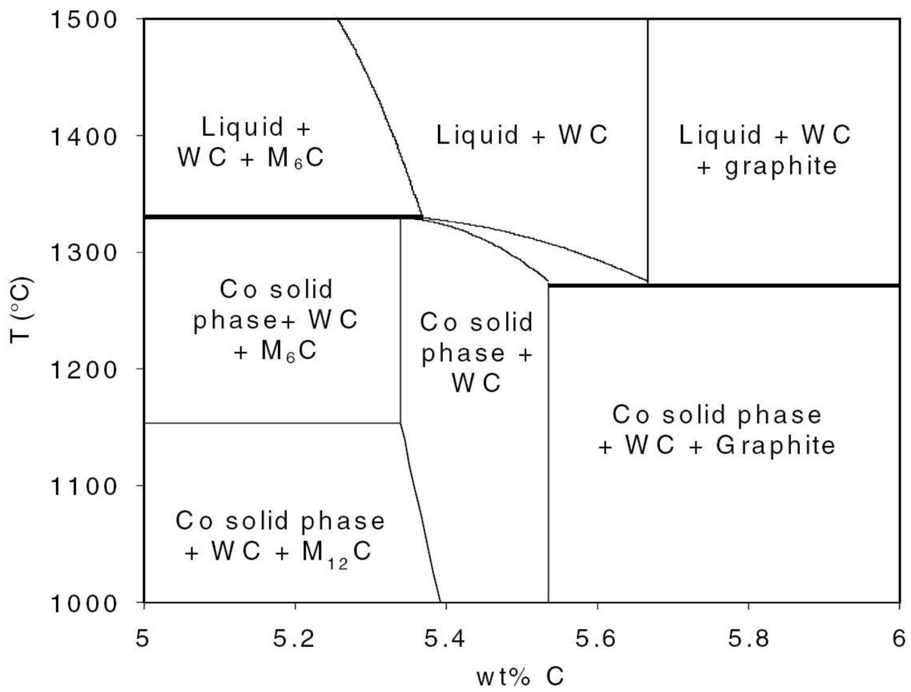

Figure 1.3: Phase diagram of the W-C-Co system at atomic ratio $W/C = 2.71$ and 10 wt% Co from [8].

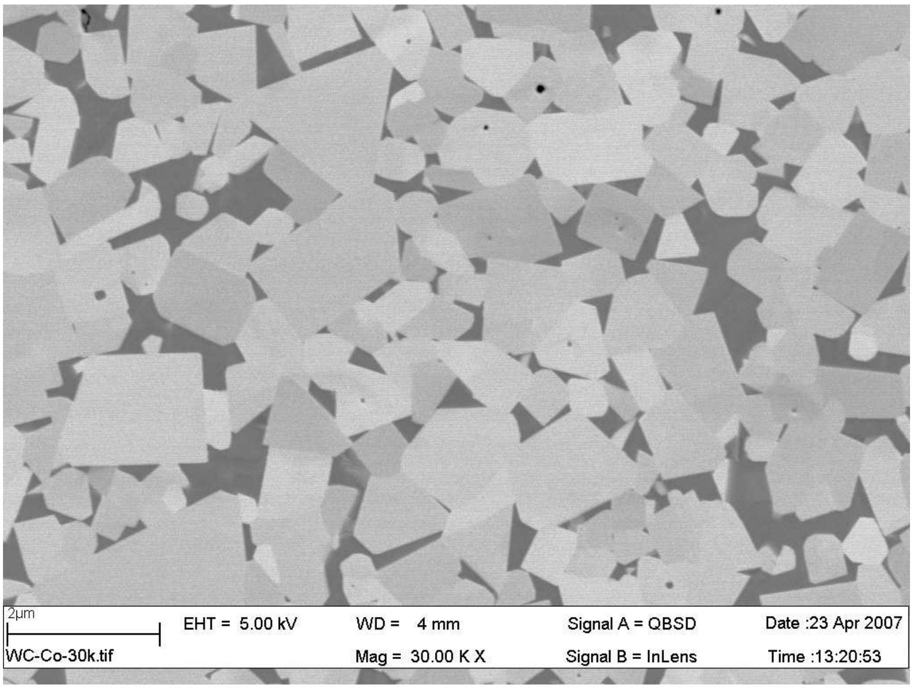

Figure 1.4: A SEM image of a typical microstructure of WC-Co without dopants. The bright parts correspond to the carbide grains. The binder is dark. Courtesy of J. Weidow.

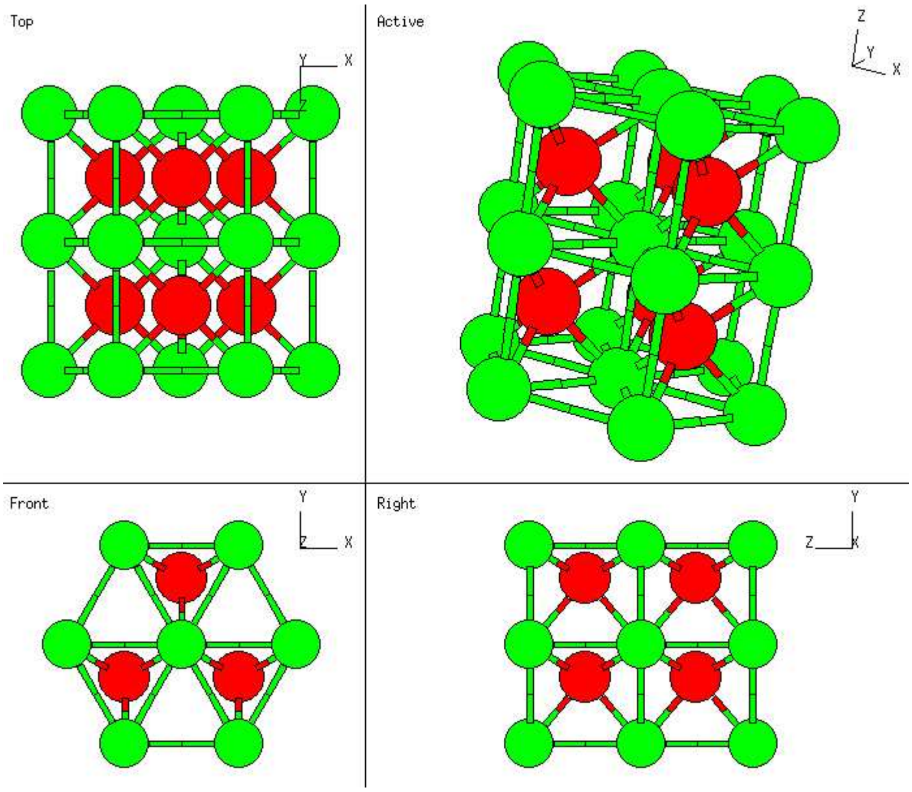

Figure 1.5: The lattice structure of hexagonal WC from [12]. The lattice vectors are $\vec{a}_1 = a\hat{x}$, $\vec{a}_2 = -a/2\hat{x} + \sqrt{3}/2\hat{y}$ and $\vec{c} = c\hat{z}$. At the bottom left, the structure is viewed from a point in the $[0001]$ direction towards the basal plane. At the top left, the structure is viewed from a point in the $[01\bar{1}0]$ direction towards a prismatic plane. At the bottom right, the $(2\bar{1}\bar{1}0)$ plane is depicted.

interplanar distance between the first and second layer of atoms. During sintering, the WC grains grow preferably on the prismatic and basal planes [9], which results in the truncated triangle shape of the grains. The equilibrium relationship in area between the two types of prismatic planes and the basal plane has been investigated both experimentally and from first-principles [11]. The results show that the grain shape attains more truncation when increasing the carbon activity.

Due to its good wetting properties, Co is the most commonly used binder in cemented carbides. The stable structure of Co is hcp up to 417 °C, where the fcc phase becomes stable. In a sintered cemented carbide, the fcc phase clearly dominates the binder. The metastable fcc phase is believed to be stabilized by dissolved tungsten and carbon [9]. A notable property of the binder phase is its large grain size. Reports of grains of millimeter size exist [13]. The large grain sizes have been explained by the scarcity of nucleation sites for the binder phase, which allows a single grain to grow substantially before facing another grain.

CHAPTER 2

Continuum description of materials

The continuum description of materials is a versatile theory applicable to such different problems as understandig crystal defects to constructing bridges and thus spans a range of valid length scales from nanometers to meters and beyond. Treating a crystal as an elastic body effectively involves the reduction of all microscopic degrees of freedom into a few material parameters, elastic constants, and replacing the discrete positions of atoms by a single displacement field.

2.1 Linear elasticity theory

In this chapter, focus will be paid to a particular form of continuum theory, namely the linear elasticity theory. The theory is widely used and has been extensively studied. The basic assumptions will be briefly introduced, and, in order to do so, we need first to consider some elementary concepts of continuum theory [14, 2]. Albeit seemingly simple, elasticity theory is in itself a complex mathematical theory.

2.1.1 Stress and strain

The theory of elasticity deals with concepts like stress, strain, and displacement. Space is assumed to be filled by a continuous medium through which forces and stresses may be transmitted. Each small volume ΔV of the continuum is acted upon by an arbritrary set of forces, which can be body forces or surface forces (tractions). To quantify these concepts, let $\hat{n}$ be the unit normal to the surface ΔS enclosing ΔV located at position $\vec{x}$ (see Figure 2.1). The material lying outside of ΔS (with respect to $\hat{n}$) will exert a force per unit area $\vec{T}$ on the material inside. The stress tensor $\sigma_{ij}(\vec{x})$

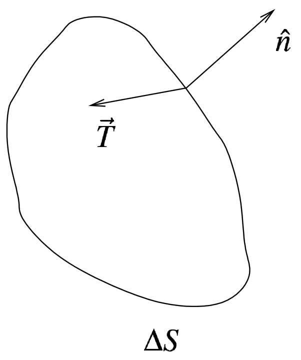

Figure 2.1: The setup used in the definition of the stress tensor σ_{ij}.

is defined, so that

$$\sum_{i=1}^{3} \sigma_{ij} n_i = T_j, \tag{2.1}$$

or $\sigma_{ij} n_i = T_j$, where double indices imply summation. Subsequently, the latter notation will be used. The diagonal elements of the stress tensor represent tensile ($\sigma_{11} > 0$) or compressive stress ($\sigma_{11} < 0$) and the off-diagonal elements represent shear stresses. For a purely hydrostatic pressure P, the stresses will be $\sigma_{ij} = -P\delta_{ij}$, so in a way, stress may be viewed as a generalization of pressure.

In the state of force equilibrium,

$$\frac{\partial}{\partial x_i} \sigma_{ij}(\vec{x}) = 0, \tag{2.2}$$

or $\sigma_{ij,i} = 0$, where $,i$ means differentiation with respect to x_i. By also letting the volume be subject to a body force density $\vec{f}$ (a typical example is gravity or electric force on a charged material), the static equilibrium condition reads

$$f_j + \sigma_{ij,i} = 0. \tag{2.3}$$

When a body is subjected to stress it will deform. A piece of material originally situated at $\vec{x}$ will be displaced to $\vec{x}' = \vec{x} + \vec{u}(\vec{x})$ (see Figure 2.2), where $\vec{u}(\vec{x})$ is the displacement field. Most often $\vec{u}$ is a continuous field, although the continuity is sometimes given up, e. g. in the case of dislocations. The displacement field gives a complete description of the deformed body. However, it does not distinguish rigid body motion from deformation. Only the latter will induce stresses in the body. Therefore, the strain tensor ε_{ij} is used as a measure of deformation. A general definition follows: Consider two neighbouring points in the body and let $\mathrm{d}s_0^2$ be the square of the distance between these prior to deformation and let $\mathrm{d}s^2$ be the distance after deformation. Now, ε_{ij} is defined as

$$\mathrm{d}s^2 - \mathrm{d}s_0^2 = 2\varepsilon_{ij}\,\mathrm{d}x_i\,\mathrm{d}x_j, \tag{2.4}$$

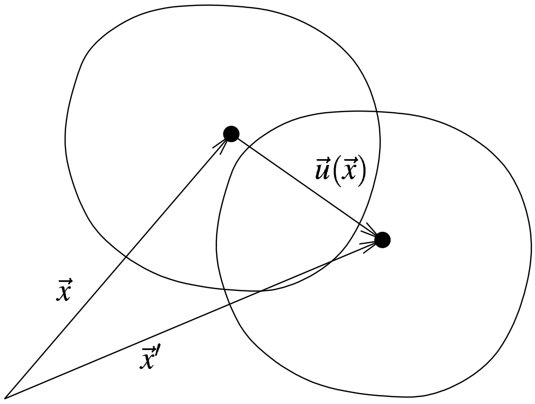

Figure 2.2: The displacement $\vec{u}(\vec{x})$.

where we take $\mathrm{d}x_i$ to be a vector between the two points in the originally undeformed body. After the deformation, the point at x_i has moved to $x_i + u_i$. Hence, $\mathrm{d}s_0^2 = \delta_{ij}\,\mathrm{d}x_i\,\mathrm{d}x_j$ and $\mathrm{d}s^2 = (\delta_{ik} + u_{k,i})(\delta_{jk} + u_{k,j})\,\mathrm{d}x_i\,\mathrm{d}x_j$. After a bit of algebra, one arrives at

$$\varepsilon_{ij} = \frac{1}{2}(u_{i,j} + u_{j,i} + u_{k,i}u_{k,j}). \tag{2.5}$$

The first assumption of *linear* elasticity is to assume that the second order term of 2.5 is negligible, which is valid when the spatial variation of $\vec{u}$ is sufficiently small. Therefore, one defines the linear strain as

$$\varepsilon_{ij} = \frac{1}{2}(u_{i,j} + u_{j,i}). \tag{2.6}$$

The diagonal elements of ε_{ij} represent expansion ($\varepsilon_{11} > 0$) or compression ($\varepsilon_{11} < 0$) and the off-diagonal elemens represent shearing.

Using the definition of linear strain 2.6 valid for infinitesimal strains, it can be shown that the work per unit volume $\mathrm{d}w$ needed to deform the small volume $\mathrm{d}V$ is $\mathrm{d}w = \sigma_{ij}\,\mathrm{d}\varepsilon_{ij}$. To proceed, we assume that the deformation is elastic, i. e. the deformation is thermodynamically reversible, so that all work performed by external forces to the body is stored as potential energy within the body, which will be released by a subsequent removal of the external forces. In reality, also plastic deformations occur in which potential energy is not conserved. A typical example is the motion of dislocations.

For thermodynamically reversible work we can write the change in internal energy per unit volume

$$\mathrm{d}e = T\,\mathrm{d}s + \sigma_{ij}\,\mathrm{d}\varepsilon_{ij}, \tag{2.7}$$

where $\mathrm{d}s$ is the change in entropy per unit volume, from which follows

$$\sigma_{ij} = \left(\frac{\partial e}{\partial \varepsilon_{ij}}\right)_s \tag{2.8}$$

for an adiabatic process. Corresponding free energies can also be introduced.

2.1.2 Materials description

Up to now, no assumptions regarding the material response have been made. To proceed, a useful simple relationship between stress and strain needs to be determined. By considering the total energy of a material from an atomistic perspective, we know that for sufficiently small forces, deformation is elastic and proportional to the force. With this motivation, *classical linear* elasticity theory postulates a generalization of Hooke's law, which states that the stresses σ_{ij} in the body are linearly related to the strains through

$$\sigma_{ij} = c_{ijkl}\varepsilon_{kl}, \tag{2.9}$$

where the coefficients c_{ijkl} are the elastic constants given by

$$c_{ijkl} = \left(\frac{\partial^2 e}{\partial\varepsilon_{ij}\partial\varepsilon_{kl}}\right)_S \tag{2.10}$$

For a given material, elastic constants can be determined from an *ab initio* calculation, albeit straight-forwardly only for $T = 0$. Experimentally, elastic constants are often measured by acoustic means [15].

Hooke's law 2.9 implies that the work per unit volume $\mathrm{d}w$ performed to deform the volume $\mathrm{d}V$ in a reversible process is

$$\mathrm{d}w = c_{ijkl}\varepsilon_{ij}\,\mathrm{d}\varepsilon_{kl}. \tag{2.11}$$

Because of the reversibility, we can define a strain energy density w, which is given by an integration of the differential work, so that

$$w = \frac{1}{2}c_{ijkl}\varepsilon_{ij}\varepsilon_{kl}. \tag{2.12}$$

When calculating the energy density, the volume element is assumed to be homogeneously deformed. A strong assumption of linear elasticity theory is that this relation holds not only for a finite volume element, but also pointwise, so that the energy stored in a body of spatially varying deformation can be obtained by summing the energy of each infinitesimal volume element as if it was homogeneously deformed, and thus the elastic energy E_{el} stored in a volume V is given by

$$E_{\mathrm{el}} = \int_V \frac{1}{2}c_{ijkl}\varepsilon_{ij}\varepsilon_{kl}\,\mathrm{d}V. \tag{2.13}$$

Through the use of 2.9, the static equilibrium conditon 2.3 concretizes into the basic field equations for displacements

$$f_i + c_{ijkl}u_{k,lj} = 0. \tag{2.14}$$

Wee see that the elastic constants contain all information about how a linear elastic body will react to external forces. The quantity c_{ijkl} is a fourth-rank tensor containing $3^4 = 81$ elements which relate the nine elements of stress σ_{ij} to the nine elements of strain ε_{kl}. However, the number of independent elements is reduced by noting that, for a body in rest, $\sigma_{ij} = \sigma_{ji}$, and from the definition of linear strain 2.6, $\varepsilon_{ij} = \varepsilon_{ji}$. These equations lead to $c_{ijkl} = c_{jikl} = c_{ijlk} = c_{jilk}$. Furthermore, since the energy e is an exact differential, the differentiation in 2.10 is independent of order in which it is performed, making $c_{ijkl} = c_{klij}$. The maximum number of independent elastic constants is hence reduced to 21. For crystals, this number is further reduced due to additional symmetries. E. g. cubic crystals have only three independent elastic constants, whereas hexagonal crystals have five.

For actual calculations, one often makes the simplifying assumption that the medium is elastically isotropic, i. e. the elastic properties are equal in all directions in which case only two independent elastic constants are needed. These constants may be chosen as the shear modulus μ and the Lamé constant λ. In an isotropic medium, $c_{ijkl} = \mu(\delta_{ik}\delta_{jl} + \delta_{il}\delta_{jk}) + \lambda\delta_{ij}\delta_{kl}$.

2.1.3 Validity of linear elasticity theory

To conclude, classic linear elasticity contains three assumptions:

- The deformed state is accurately described by the linear strain 2.6.
- Hooke's law holds, from which follows that the elastic energy is proportional to the square of the strain.
- The elastic energy of an arbitrarily deformed body is given by treating each volume element as if it was part of a homogeneously deformed body.

The validity of Hookes' law can for a given material easily be tested. In Figure 2.3 the elastic energy of a uniformly compressed and expanded cell of bcc-Fe is given both by DFT and EAM calculations and elasticity theory. We see that the agreement is reasonable up to a few percent of expansion. The plot shows some general deficits of elasticity theory, namely that it usually underestimates energy due to compression, but overestimates energy due to expansion. One should note, that for the largest deformations, also the DFT and EAM results are questionable. To get a better agreement between elasticity theory and atomistic modelling, one could add higher-order terms to the energy density 2.12. For the description of inhomogenously strained materials, corrections that take the gradient of strain into account would be benificial.

2.2 Solving the equations

Now that all relevant quantities are defined, attention can be paid towards the more difficult business of solving the basic field equations 2.14 for a given set of boundary conditions. As in many other area of physics, Green's functions provide a way of reaching the answer. In this context, the Green's function G_{ij} is defined as follows:

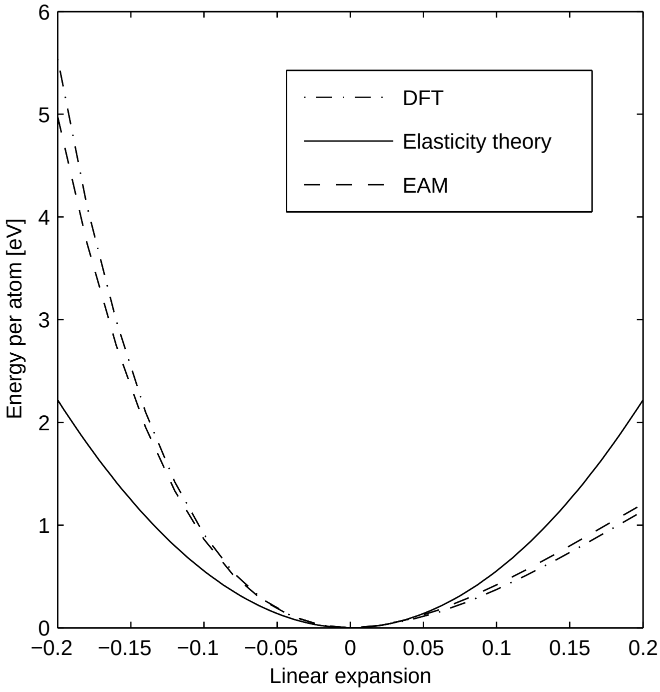

Figure 2.3: Elastic energy per atom of a uniformly expanded cell of bcc-Fe as given by different methods.

Consider a point force $\vec{F}$ acting at the point $\vec{x}'$. The displacement at $\vec{x}$ is then given as $u_i = G_{ij}(\vec{x}-\vec{x}')F_j$.

In the case of a linear anisotropic, homogeneous, and infinitely extending body, the Green's function can be shown to be (see [14] for a derivation)

$$G_{ij}(\vec{x}-\vec{x}') = -\frac{1}{4\pi\left|\vec{x}-\vec{x}'\right|}Q_{ij}, \tag{2.15}$$

where Q_{ij} is an orientation dependent quantity to be defined below. This Green's function is of use when dealing with point defects and inclusions. For other cases, the Green's functions have to be modified in order to cope with the boundary conditions. One such case is a semi-infinite body with a free surface, where a single-point force cannot give rise to a traction-free surface.

To solve a general elasticity problem numerically, a finite element method is most often the preferred choice. Today, an abundant number of both commercially and free computer codes exist for this purpose.

2.2.1 Sextic and integral formalism

In the appended papers, we have studied the interface energetics between semicoherent interfaces residing misfit dislocations. For a special class of elastic problems including dislocations and other two-dimensional (plane) problems, a methodology involving complex variables was developed by Eshelby and Stroh [16, 17], the so called sextic formalism. It was later cast into a slightly different form, the integral formalism, by Lothe and coworkers [18, 19, 20].

Let us begin by looking at the sextic formalism. The problem setup involves an infinite homogeneous anisotropic elastic body. Let $\vec{m}$, $\vec{n}$, and $\vec{t}$ be three mutually orthogonal unit vectors and let $\vec{x}$ be a point in the body. The method deals with problems where the elastic fields do not depend on $\vec{t}\cdot\vec{x}$. The solution to the basic field equation 2.14 in absence of body forces,

$$c_{ijkl}u_{k,lj} = 0, \tag{2.16}$$

is sought among the functions

$$u_k = A_k f(\vec{m}\cdot\vec{x} + p\vec{n}\cdot\vec{x}), \tag{2.17}$$

where A_k is a complex vector, p is a complex constant, and f is an analytical function. By letting $\lambda = \vec{m}\cdot\vec{x} + p\vec{n}\cdot\vec{x} = m_i x_i + p n_i x_i$, 2.16 holds if

$$c_{ijkl}(m_i + pn_i)(m_l + pn_l)A_k \frac{\mathrm{d}^2 f}{\mathrm{d}\lambda^2} = 0. \tag{2.18}$$

Non-trivial solutions exist when $\det\left(c_{ijkl}(m_i + pn_i)(m_l + pn_l)\right) = 0$, which is a sixth-order polynomial in p, and thus have six roots. Associated with each root p_α is an eigenvector $A_{k\alpha}$. The most general solution to 2.18 is a linear combination of the solutions corresponding to each p_α, i. e.

$$u_k = \sum_{\alpha=1}^{6} A_{k\alpha} D_\alpha f(\vec{m}\cdot\vec{x} + p\vec{n}\cdot\vec{x}), \tag{2.19}$$

where the D_α are constants to be determined by the boundary conditions at hand.

The theory is further extended by defining an associated vector $L_{j\alpha} = -n_i c_{ijkl}(m_l + p_\alpha n_l) A_{k\alpha}$. The vectors A and L are known as the Stroh eigenvectors. Interesting orthogonality, completeness and invariance relations of these vectors have been derived, and are put to use in the so called integral formalism. In the integral formalism, the awkward solving of sixth-order polynomials is replaced by angle-dependent integrals. E. g. the quantity Q_{ij} mentioned above in relation to the Green's function of a linear anisotropic, homogeneous, and infinitely extended body, can be expressed in two ways,

$$Q_{ij} = \sqrt{-1}\sum_{\alpha=1}^{6} \pm A_{i\alpha} A_{j\alpha} = -\frac{1}{2\pi}\int_0^{2\pi} (nn)^{-1}_{ij}\, \mathrm{d}\omega, \tag{2.20}$$

where the first form is in the sextic formalism and the second in the integral formalism. In the sextic formalism expression, the upper (lower) sign apply for $\alpha = 1,2,3(4,5,6)$ and the ordering of $A_{k\alpha}$ is such that $\mathrm{Im} p_\alpha > 0$ for $\alpha = 1,2,3$, and $\mathrm{Im} p_\alpha < 0$ for $\alpha = 4,5,6$. In the integral formalism expression, the matrix $(nn)_{jk} = n_i c_{ijkl} n_l$ and the angle ω is the angle of rotation of $\vec{n}$ and $\vec{m}$ around some fixed vector in the plane spanned by $\vec{n}$ and $\vec{m}$. Among the advantages of the integral formalism is that it avoids the problem of root degeneracy which may occur in the sextic formalism, e. g. in the important case of isotropy.

2.2.2 Application to dislocations

The theory described in the previous section fits well for the mathematical description of an infinitely long straight dislocation, whose elastic field is a planar object, which has no variation along the dislocation line. In order to obtain the displacement field of the dislocation, one needs to find constants D_α and a function f which accurately yields the correct boundary conditions appropriate for a dislocation.

A dislocation is described by its Burgers vector $\vec{b}$, which is a measure of the discontinuity of the displacement field associated with the dislocation. If we imagine $\vec{m}$ pointing to the right of the paper, $\vec{n}$ to the top, and $\vec{t}$ out of the paper, we can choose to make a cut halfway into the material along the halfplane $\vec{m}\cdot\vec{x} > 0, \vec{n}\cdot\vec{x} = 0$. The cut ends at the dislocation line $\vec{t}$. Before welding the parts together, we displace the lower part relative to the upper part by $\vec{b}$. The Burgers condition then reads

$$u_i(\vec{m}\cdot\vec{x} > 0, \vec{n}\cdot\vec{x} = 0^-) - u_i(\vec{m}\cdot\vec{x} > 0, \vec{n}\cdot\vec{x} = 0^+) = b_i. \tag{2.21}$$

A function with this property is

$$u_i = \frac{1}{2\pi\sqrt{-1}}\sum_{\alpha=1}^{6} A_{i\alpha} D_\alpha \ln(\vec{m}\cdot\vec{x} + p_\alpha \vec{n}\cdot\vec{x}), \tag{2.22}$$

where the branch cut of the logarithmic function is chosen along $\vec{m}\cdot\vec{x} > 0, \vec{n}\cdot\vec{x} = 0$. The boundary conditions for the D_α is firstly the Burgers condition

$$\sum_{\alpha=1}^{6} \pm A_{i\alpha} D_\alpha = b_i, \tag{2.23}$$

which gives three equations for the six unknowns D_α. Secondly, further equations can be acquired by studying the curve integral

$$T_j = \oint_C \sigma_{ij} N_j \, \mathrm{d}s, \tag{2.24}$$

where C is the curve around the dislocation line $\vec{t}$ in a positive sense and σ_{ij} is the stress from the dislocation. The integral represents the net traction associated with the dislocation and, with a line force $\vec{f}$ acting along the dislocation line, the integral 2.24 reduces to

$$\sum_{\alpha=1}^{6} \pm L_{i\alpha} D_\alpha = -f_i. \tag{2.25}$$

For a pure dislocation $\vec{f} = 0$. The two equations 2.23 and 2.25 completely specifies the displacement 2.22. One may note, that this dislocation, known as a Volterra dislocation, is a highly idealized one, in the sense that it is localized only to the dislocation line, on which the strain diverges and therefore it is applicable only to a true continuum. Eshelby [21] considers dislocations to be built by a distribution of Volterra dislocations, each one with an infinitesimal Burgers vector $\vec{b}$. This view is more appropriate when dealing with lattices, and is put to use in the Peierls-Nabarro model of dislocations (see 4.1).

The situation treated in the appended papers is a bit more involved than the problem of a dislocation in a homogeneous material described above, since we studied dislocations at the interface between two dissimilar materials. It is, however, possible to construct a function with the same form as 2.22, but with different constants D_α (and p_α) for each half-space. Together with the Burgers condition and the zero net traction, one also applies the boundary conditions of continuous displacements along $\vec{m}\cdot\vec{x} < 0$ and continuous traction over the whole interface, which in total results in twelve conditions needed for the twelve unknowns [22].

Generally, the elastic energy per unit length due to a dislocation is found by use of 2.13. However, when integrating over all space, the energy of an ideal dislocation is found to be logarithmically divergent. The solution is to consider a hollow cylinder of inner radius r_0 and outer radius R around the dislocation. By the use the divergence theorem [14], the energy E_{disl} contained within the cylinder is found to be

$$E_{\mathrm{disl}} = E \ln \frac{R}{r_0}, \tag{2.26}$$

where

$$E = b_i B_{ij} b_j. \tag{2.27}$$

The quantity E is called the prelogarithmic energy factor [2]. For a dislocation in a homogeneous material, the expression for B_{ij} in the sextic formalism is

$$B_{ij} = -\frac{1}{4\pi\sqrt{-1}} \sum_{\alpha=1}^{6} \pm L_{i\alpha} L_{j\alpha}. \tag{2.28}$$

Often it is more convenient to define the energy coefficient K_{ij} of a dislocation, which equals $4\pi B_{ij}$ resulting in $E = b_i K_{ij} b_j / 4\pi$. In an isotropic material, an edge dislocation has energy coefficient $K_\mathrm{e} = \mu/(1-\nu)$, where ν is the Poisson's ratio, and a screw dislocation $K_\mathrm{s} = \mu$. For a dislocation at an interface, similar expressions exist [22].

Returning to the energy of a dislocation 2.26, there are two parameters R and r_0 which need to be defined. A common choice is to let $r_0 \approx b$ and R to be the average grain size of the material. However, for comparison of different dislocations it is more well-defined to consider the energy factor E.

CHAPTER 3

Atomistic description of materials

Both the continuum and atomistic description of materials seek to measure the energy of a physical system as a function of the system's geometry. Whereas the geometric description in the continuum description is locked into a displacement field, the atomistic description deals with all atomic coordinates of the system.

For a complete microscopic description of the total energy, the quantum mechanical ground state of the system is found by taking into account all nuclear and electronic degrees of freedom. The first step towards a tractable atomistic description is the Born-Oppenheimer approximation [23], which assumes that the many body wave function including both electrons and nuclei may be separated into an electron and a nuclear part. Because of the large ratio between the nucleus and electron masses, it is assumed that the electrons instantaneously adapt to a change in nuclear positions and hence that the nuclei always move on the potential energy surface given by the electronic ground state. The electronic wave function will depend only parametrically on the nuclear positions. In most applications, it is not necessary to calculate a nuclear wave function. Instead, the energy and motion of the nuclei are described classically. One is therefore left with the task of finding an energy function

$$E = E(\vec{R}_\alpha), \tag{3.1}$$

where $\vec{R}_\alpha$ is a set of all atomic coordinates of the system.

Basically, there are two different ways of deriving the potential $E(\vec{R}_\alpha)$. The most fundamental one is the first-principles method, which gives $E(\vec{R}_\alpha)$ with no other input than the atomic species and positions. It is often a reliable, yet computationally demanding method. The alternative is to find $E(\vec{R}_\alpha)$ semi-empirically, where a functional form for the potential is guessed from physical reasoning and parameters are fitted to experiments and/or first-principles calculations. In the subsequent sections, examples from both methods will be mentioned.

Before describing atomistic calculations in detail, it is instructive to see how the continuum description of a material as treated in Chapter 2 can be derived from a first-principles theory. Assuming that the energy $E(\vec{R}_\alpha)$ is fully known from first-principles, how does one arrive at linear elasticity theory? The first step [23] in finding the connection is to expand the energy $E(\vec{R}_\alpha)$ to second order around its equilibrium value E_0, giving

$$E = E_0 + \sum_\alpha \frac{\partial E}{\partial u_{i\alpha}} u_{i\alpha} + \sum_{\alpha,\beta} \frac{1}{2} u_{i\alpha} \frac{\partial^2 E}{\partial u_{i\alpha} \partial u_{j\beta}} u_{j\beta} + O(u_{i\alpha} u_{j\beta} u_{k\gamma}), \tag{3.2}$$

where $u_{i\alpha}$ is the displacement of atom α. Note that the second term of 3.2 is zero, due to force equilibrium. By assuming that the atomic displacements vary only slightly from lattice site to lattice site, it is possible to consider a continuous displacement field $\vec{u}(\vec{x})$ that takes the value $\vec{u}_\alpha$ at lattice site α, and additionally, under the same assumption,

$$u_{j\beta} = u_{j\alpha} + (R_{i\beta} - R_{i\alpha}) \left. \frac{\partial u_j}{\partial x_i} \right|_{\vec{x}=\vec{R}_\alpha}, \tag{3.3}$$

for nearby α and β. With these simplifications, the expansion 3.2 reduces to

$$E = E_0 + \frac{1}{2} \sum_\alpha u_{j,i}\big|_{\vec{x}=\vec{R}_\alpha} E_{ijkl}\, u_{l,k}\big|_{\vec{x}=\vec{R}_\alpha}, \tag{3.4}$$

where

$$E_{ijkl} = -\sum_\beta \frac{1}{2} R_{i\beta} \frac{\partial^2 E}{\partial u_{j0} \partial u_{l\beta}} R_{k\beta}. \tag{3.5}$$

In deriving E_{ijkl}, reference is made to the fact that the atoms are positioned on a Bravais lattice, which makes $\partial^2 E/(\partial u_{j\alpha} \partial u_{i\beta})$ invariant under a translation of α and β with a lattice vector. Without a Bravais lattice, E_{ijkl} would depend on α.

To proceed, one demands that the energy should be constant for an arbitrary rotation of the material. This implies that the energy depends only on a symmetrical combination $\varepsilon_{ij} = \frac{1}{2}(u_{i,j} + u_{j,i})$, which is recognized as the linear strain. By replacing the sum of 3.4 with an integral, we arrive at an expression for the energy which is identical (apart from the constant energy shift E_0) to 2.13 derived from linear elasticity theory, namely

$$E = E_0 + \int_V \frac{1}{2} \varepsilon_{ij} c_{ijkl} \varepsilon_{kl} \, \mathrm{d}V, \tag{3.6}$$

where V is the volume of the crystal and the elastic constants c_{ijkl} are reintroduced, but here with the definition

$$c_{ijkl} = \frac{1}{4V} \left(E_{ijkl} + E_{jikl} + E_{ijlk} + E_{jilk} \right). \tag{3.7}$$

3.1 First-principle methods

At the basis of all first-principles methods lies the time-independent Schrödinger equation, which, under the Born-Oppenheimer approximation, takes the form

$$H\Psi(\vec{r}_\beta;\vec{R}_\alpha) = E(\vec{R}_\alpha)\Psi(\vec{r}_\beta;\vec{R}_\alpha), \tag{3.8}$$

The set of electronic coordinates is denoted $\vec{r}_\beta$ and explicit reference is made to the fact that the energy and wavefunctions are parametrically dependent on the nuclear coordinates $\vec{R}_\alpha$. The Hamiltonian consists of three parts

$$H = T + V_{\text{ee}} + V_{\text{ext}}, \tag{3.9}$$

where T is the kinetic energy, V_{ee} the electron-electron interaction, and V_{ext} the potential from the nuclei including also the constant energy shift due to the interaction between the nuclei themselves.

For a piece of real material containing an Avogadrian number of particles, solutions to the Schrödinger equation are computionally not feasible. In fact, only a handful electrons can be treated exactly. The problematic part is the electron-electron interaction V_{ee} which hinders the total wavefunction from decomposing into a product of one-particle wavefunctions. An approximate treatment or neglect of electron-electron interaction is therefore a common feature of many electron structure calculations.

There are two choices of fundamental variable for characterizing an electronic system in the ground state: the wavefunction or the electronic density. In the Hartree and Hartree-Fock methods, the former is used, whereas density functional theory (DFT) uses the latter. DFT is, in principle, capable of treating the electron-electron interaction exactly, but in practice it must be approximated. The applicability of DFT depends strongly on the accuracy of these approximations. In the appended papers, we have used DFT to evaluate the energetics of interfaces. In the next section, some basics of DFT will be given.

3.1.1 Theoretical background of density functional theory

Since its formulation in the 1960s, DFT has grown to become one the most successful computational methods in atomistic calculations. A thorough introduction is given by Martin [24]. The basis of DFT is formed by two theorems of Hohenberg and Kohn [25]. The first Hohenberg-Kohn theorem states that the electron density may be used in place of the potential as the basic function uniquely characterizing the system, or in other words, the ground state density $n(\vec{r})$ uniquely determines the external potential $V_{\text{ext}}(\vec{r})$, up to an arbitrary constant. According to the variation principle, the ground state energy E is found by

$$E = \min_{\Psi}\langle\Psi|T + V_{\text{ee}} + V_{\text{ext}}|\Psi\rangle, \tag{3.10}$$

where the minimization is over all antisymmetric N electron wavefunctions Ψ. However, it would be easier to search for an electron density $n(\vec{r})$, since this is a function of only three space variables compared to the $3N$ coordinates of the wavefunction. By defining a functional

$$F[n] = \min_{\Psi \to n} \langle \Psi | T + V_{\mathrm{ee}} | \Psi \rangle, \tag{3.11}$$

where the minimization is over all antisymmetric wavefunctions Ψ that gives a particular density n, the search in 3.10 can be reformulated into [26]

$$E = \min_{n} \left(F[n] + \int V_{\mathrm{ext}}(\vec{r}) n(\vec{r})\, \mathrm{d}\vec{r} \right), \tag{3.12}$$

where the minimization is over all N electron charge densities n. Now, the second Hohenberg-Kohn theorem states that there exists a single universal functional $F[n]$, i. e. it is independent of the external potential, which should be evident from 3.11. By introducing a functional $E[n]$ (defined as in 3.12 excluding the minimization) and a Lagrange multiplier μ for the fixed particle number constraint,

$$N = \int \mathrm{d}\vec{r}\, n(\vec{r}), \tag{3.13}$$

one seeks to minimize $E[n] - \mu N$ through the Euler-Lagrange's equation

$$\frac{\delta F}{\delta n(\vec{r})} + V_{\mathrm{ext}}(\vec{r}) = \mu. \tag{3.14}$$

This would be a convenient way of determining the ground state properties of any external potential if only the functional $F[n]$ was known. It is, however, not and the importance of the Hohenberg-Kohn theorems could therefore seem to be primarily theoretical.

Luckily, Kohn and Sham [27] found a mathematically tractable way of solving the original many-body problem. In the Kohn-Sham formulation, the starting point is to separate $F[n]$ into different parts,

$$F[n] = T_s[n] + E_{\mathrm{H}}[n] + E_{\mathrm{xc}}[n], \tag{3.15}$$

where $T_s[n]$ is the kinetic energy functional for *non-interacting* electrons, and $E_{\mathrm{H}}[n]$ is the Hartree energy, which is the electrostatic energy stored in a charge density $n(\vec{r})$, given by

$$E_{\mathrm{H}}[n] = \frac{1}{2} \int \int \mathrm{d}\vec{r}\mathrm{d}\vec{r}' \frac{n(\vec{r})n(\vec{r}')}{|\vec{r} - \vec{r}'|}. \tag{3.16}$$

The remaining term of 3.15, $E_{\mathrm{xc}}[n]$, is called the exchange and correlation energy, which should capture all errors arising from replacing $T + V_{\mathrm{ee}}$ by $T_s + E_{\mathrm{H}}$. The essential result of the Kohn-Sham formulation, is that the Euler-Lagrange's equation 3.14 for the functional 3.15 is *exactly* fulfilled for a set of non-interacting electrons obeying the one-electron Schrödinger equation (in atomic units),

$$\left(-\frac{1}{2} \nabla^2 + V_{\mathrm{KS}}(\vec{r}) \right) \phi_i(\vec{r}) = \varepsilon_i \phi_i(\vec{r}) \tag{3.17}$$

where V_{KS} is a density-dependent potential, given by

$$V_{\mathrm{KS}}(\vec{r}) = V_{\mathrm{ext}}(\vec{r}) + \frac{\delta E_{\mathrm{H}}[n(\vec{r})]}{\delta n(\vec{r})} + \frac{\delta E_{\mathrm{xc}}[n(\vec{r})]}{\delta n(\vec{r})}. \tag{3.18}$$

From a comparison of 3.15 and 3.17 it is deduced that

$$E = \sum_i f_i \varepsilon_i - E_{\mathrm{H}}[n(\vec{r})] + E_{\mathrm{xc}}[n(\vec{r})] - \int \mathrm{d}\vec{r}\, n(\vec{r}) \frac{\delta E_{\mathrm{xc}}[n(\vec{r})]}{\delta n(\vec{r})}, \tag{3.19}$$

where f_i is the occupational number of the electronic Kohn-Sham state i. To find the energy E in practice, one has to solve the Kohn-Sham equation 3.17 iteratively, since V_{KS} depends on the solution itself. Starting with a reasonable first guess for the density, the equations are solved until self-consistency.

Some points are worth noting. In principle, the Kohn-Sham equations are exact and yield the exact density. Since the equations are single-particle equations, they are much easier to solve than the original coupled Schrödinger equation. In return, however, the electron-electron interaction energy has to be approximated. By separating the interaction into $E_{\mathrm{H}}[n]$ and $E_{\mathrm{xc}}[n]$, where the former is known exactly, it turns out that the latter is more amenable to efficient approximations.

3.1.2 Exchange correlation approximations

A first approximation of $E_{\mathrm{xc}}[n]$ was suggested already in the original Kohn-Sham paper [27] and is known as the local density approximation (LDA). In the LDA, the exchange correlation energy at a point $\vec{r}$ is set to equal the exchange correlation energy $\varepsilon_{\mathrm{xc}}(n)$ of a homogeneous electron gas of density $n(\vec{r})$, making

$$E_{\mathrm{xc}}[n] = \int \mathrm{d}\vec{r}\, n(\vec{r}) \varepsilon_{\mathrm{xc}}\left(n(\vec{r})\right). \tag{3.20}$$

For the homogeneous electron gas, an exact expression can be derived for the exchange energy by calculating a Fock integral for a Slater determinant of orbitals. This motivates that the exchange correlation energy is split into two parts: $\varepsilon_{\mathrm{xc}} = \varepsilon_{\mathrm{x}} + \varepsilon_{\mathrm{c}}$. The correlation part can be found from Monte Carlo simulations [28].

To treat spin-polarized systems, one introduces spin densities, such that

$$n = n_{\uparrow} + n_{\downarrow} \tag{3.21}$$

(see e. g. [24]), where $n_{\uparrow}$ ($n_{\downarrow}$) is the density of spin-up (down) electrons. Generalization to an arbitrary direction is possible. The local spin density approximation (LSDA) is the spin-polarized generalization of LDA. The kinetic and exchange energy in the LSDA can be found by spin-scaling arguments. The correlation energy as a function of spin-polarization must, however, be extracted from Monte Carlo calculations.

LDA has proven to be a surprisingly good approximation for exchange and correlation, at least in solids. The reason is that exchange and correlation effects are short-ranged and one can therefore expect that LDA will work best for solids resembling a homogeneous gas and worst for inhomogeneous systems, like free atoms or molecules. However, LDA also works for some cases of varying density, which is considered to be a consequence of the fact that it describes the exchange-correlation hole created around an electron correctly according to certain sum rules [24].

To better deal with inhomogeneous systems, a more elaborate approximation includes also the gradients of the density. In the popular generalized gradient approximations (GGA), the exchange-correlation energy takes the form

$$E_{\mathrm{xc}}[n] = \int \mathrm{d}\vec{r}\, n(\vec{r})\varepsilon_{\mathrm{xc}}(n(\vec{r}), \nabla n(\vec{r})). \tag{3.22}$$

This functional form is called semi-local, since it takes account of the density not just at $\vec{r}$, but also in the infinitesimal vicinity of $\vec{r}$. In the beginning of the DFT era, it was believed that the gradient expansion approximation (GEA), which expands the true exchange correlation functional with an increasing number of density differentiations and powers would lead to better accuracy. This is, however, not the case which has lead to a diversity in the formulation of GGAs. In the appended papers, the GGA version by Perdew and Wang (PW91) [29] has been used.

3.1.3 Pseudopotentials and plane-wave implementation

Despite the simplification introduced by the Kohn-Sham approach to DFT, one is still left with the quite overwhelming problem of solving the Kohn-Sham equations for all electrons of the system. For isolated atoms and molecules this is doable by using localized basis sets. For solids, however, the natural choice of basis set is plane waves. Consequently, periodical boundary conditions are imposed on the computational cell. Then, the conditions for Bloch's theorem are fulfilled, meaning that the wavefunctions can be written as

$$\Psi_{n,\vec{k}}(\vec{r}) = u_{n,\vec{k}}(\vec{r}) e^{i\vec{k}\cdot\vec{r}}, \tag{3.23}$$

where $u_{n,\vec{k}}(\vec{r})$ has the periodicity of the lattice, n is the band index, and $\vec{k}$ is a vector in the first Brillouin zone. Due to the periodicity, $u_{n,\vec{k}}(\vec{r})$ can be expanded in plane waves with wave vectors of the reciprocal lattice,

$$u_{n,\vec{k}}(\vec{r}) = \sum_j c_{n,\vec{k},j} e^{i\vec{G}_j\cdot\vec{r}}. \tag{3.24}$$

To create a finite basis set, only reciprocal lattice vectors of kinetic energy $\left|\vec{k}+\vec{G}\right|^2/2$ less than some predefined cutoff are included in the sum.

When modeling defects, the system often lacks periodicity in one or more dimensions. Defects are therefore treated by imposing an artificial periodicity, e. g. a surface is modeled by creating a slab and a layer of vacuum, which in fact yields two surfaces. Of course, care has to be taken to choose the slab size thick enough to avoid interaction between the two surfaces.

The drawback of using a delocalized basis set such as plane waves, is the need of a large basis set to accurately describe localized functions, such as the charge density in the vicinity of the nucleus. Often, only the valence electrons are therefore included in the DFT calculation. The effect of the core electrons and nucleus is replaced by a pseudopotential, which is chosen such that the true all electron wavefunction and the pseudo wavefunction coincide outside some appropriately chosen core radius. Using this construction, the often complicated structure of the true wavefunction near the nuclei is simplified into a smoother version, which allows a smaller basis set. Luckily, the core electron states are often negligibly affected by the atomic environment under reasonable conditions (exceptions being e. g. extreme pressures), and only valence electrons contribute to chemical bonding, which explains the success of the pseudopotential approach for describing actual solid-state properties of materials.

3.2 Model potentials

Although bonding between atoms is of quantum mechanical origin, where electrons act as a glue between the positively charged nuclei, it is often desirable to remove the explicit dependence of the electrons on the total energy, and only consider the energy as a function of atomic coordinates, where the electrons are effectively integrated into the energy function $E(\vec{R}_\alpha)$.

3.2.1 Pair potentials

The simplest example of an energy function $E(\vec{R}_\alpha)$ takes the form

$$E = \sum_{\substack{i,j \\ i<j}} V(R_{ij}), \tag{3.25}$$

where V is a pair potential and R_{ij} is the distance between atom i and j. The total energy is here decomposed into contributions from interactions between pair of atoms. The most familiar and thoroughly investigated pair potential is the Lennard-Jones potential, where

$$V(R_{ij}) = 4\varepsilon\left[\left(\frac{\sigma}{r}\right)^{12} - \left(\frac{\sigma}{r}.\right)^{6}\right]. \tag{3.26}$$

ε is the depth of and σ the distance where the potential changes sign from repulsive to attractive. The potential can be used to study systems of closed-shell atoms, where interaction occurs mainly due to polarization.

The advantage of pair potentials is the ability to quickly calculate total energies and forces. Therefore they are attractive for molecular dynamics simulations and thermodynamical calculations. The physical justification of their use is however weak and the problems are both qualitative and quantitative. As an example of the former, the energy of a bond between two atoms will always be the same, regardless of the environment. Quantitatively, pair potentials cannot accurately describe even the simple case of elastic deformation of a solid. A material of cubic symmetry, will, using pair potentials, always fulfill the so called Cauchy relation, $c_{12} = c_{44}$.

3.2.2 Embedded atom method

To remedy some of the mentioned shortcomings of pair potentials, it is necessary to account for the environmental dependence of the bond strength. This can be accomplished by including an additional term to the total energy function,

$$E = \sum_{\substack{i,j \\ i<j}} V(R_{ij}) + \sum_{i} F(\rho_i), \tag{3.27}$$

where the physical interpretation and expression for $F(\rho_i)$ varies among different workers. This functional form was used extensively in the 1980s to predict properties of defects in solids, and has appeared with different names such as Finnis-Sinclair potential [30], effective medium theory [31] (EMT), and embedded atom method [32] (EAM).

The Finnis-Sinclair potential is derived from a tight-binding model. By utilizing information about the second moment μ_2 of the local density of states, it turns out that $F(\rho_i)$ is proportional to the square root of μ_2. It is further argued that μ_2 can be taken as a sum of pairwise interactions between neighboring atoms, which leads to a functional form $F(\rho_i) \propto \sqrt{\rho_i}$, where ρ_i is given by an expression similar to 3.28 below.

The physical idea behind the EMT and EAM is that there is a certain energy cost $F(\rho_i)$ associated with placing an atom in an electron gas. If one considers a metal in a periodic structure, one can think of one particular atom i as being embedded in the electron density ρ_i given by the rest of the atoms. In EMT, $F(\rho_i)$ is determined explicitly from DFT by calculating the energy of placing an atom in jellium at density ρ_i. In EAM, however, $F(\rho_i)$ is determined semi-empirically and the density at atom i is taken to be a sum

$$\rho_i = \sum_{j \neq i} f(R_{ij}). \tag{3.28}$$

of contributions $f(R_{ij})$ from its neighbors.

By combining a pair potential to describe the Coulombic interaction between the nuclei with an embedding energy for the electron gas, EAM has successfully been used for modeling metals of non-directional bonding. From a computational point of view, EAM is only twice as time-consuming as a simple pair potential.

In one of the appended papers, an EAM implementation for Fe has been used [33]. In this implementation, the energy function is fitted to cohesive energy, lattice parameter, elastic constants, and vacancy formation energy. The contribution to the electron density at atom i from a neighboring atom j is chosen as $f(R_{ij}) = \exp(-\beta R_{ij})/R_{ij}$, which matches the functional form of the Thomas-Fermi screening function. By first adopting the pair potential $V(R_{ij})$, the embedding energy $F(\rho_i)$

is found by making a uniform expansion and compression of the lattice and fitting the result to Rose's expression [34] for the total energy as a function of lattice parameter. The Rose zero temperature equation of state is based on experimental pressure-volume data and has the form

$$E(a^*) = -E_{\mathrm{coh}}(1+a^*)\exp(-a^*), \tag{3.29}$$

where E_{coh} is the cohesive energy and the dimensionless parameter $a^* = (a-a_0)/l$. a is the actual lattice parameter, a_0 the lattice parameter in equilibrium, and l is a length scale given by $l^2 = a_0^2 9B\Omega/E_{\mathrm{coh}}$, where B is the bulk modulus and Ω the atomic volume of the material.

3.2.3 Angular dependent and bond-order potentials

To treat materials of covalent bonding, it is often necessary to include angular terms. A well-known example of an angular dependent potential is the Stillinger-Weber potential [35] for Si. It has its origin in the expansion of the energy $E(\vec{R}_\alpha)$ as a sum of additive one-body, two-body, three-body etc. contributions. In the Stillinger-Weber potential, the three-body contribution $V_3(\vec{R}_i,\vec{R}_j,\vec{R}_k)$ is taken to be a sum of functions of the form $h(R_{ij},R_{jk},\theta_{ijk})$, where θ_{ijk} is the angle between $\vec{R}_i$ and $\vec{R}_k$ measured from $\vec{R}_j$. $h(R_{ij},R_{jk},\theta_{ijk})$ contains a factor $(\cos\theta_{ijk}+1/3)^2$, which minimizes at the tetrahedral angle of $\theta_{ijk} \approx 109.5^\circ$. Thus the Stillinger-Weber potential stabilizes the diamond structure, which cannot be done by a simple pair potential.

The Stillinger-Weber potential, as well as any other implementation of additive N-body potentials, lacks the environmental dependence of bonding energy that EAM incorporates. This motivated Tersoff [36] to formulate a bond order potential (BOP) that takes the coordination number into account when calculating the bond strength (bond order). In the BOP, the energy is written

$$E = \frac{1}{2}\sum_{i\neq j} V(R_{ij}), \tag{3.30}$$

where

$$V(R_{ij}) = f_C(R_{ij})\left(a_{ij}f_R(R_{ij}) + b_{ij}f_A(R_{ij})\right). \tag{3.31}$$

Here f_R is a repulsive energy, f_A an attractive bonding energy, and f_C a cutoff function. a_{ij} is a range-limit function of no physical interest. The new physics comes into b_{ij}, which is written

$$b_{ij} = \left(1+\beta^n\zeta_{ij}^n\right)^{-\frac{1}{2n}} \tag{3.32}$$

where environmental and angular dependence enter through

$$\zeta_{ij} = \sum_{k\neq i,j} f_C(R_{ik})g(\theta_{ijk})\exp(\lambda^3(r_{ij}-r_{ik})^3) \tag{3.33}$$

and

$$g(\theta) = 1 + \frac{c^2}{d^2} - \frac{c^2}{d^2+(h-\cos\theta)^2}. \tag{3.34}$$

BOP has the ability of treating both metallic and covalent systems and can therefore be used where the more simple EAM potentials fail. In fact, BOP can be considered as an extension of EAM [37]. One example of successful application of BOP is Ga-As [38], where the potential must describe both the metallic pure Ga phase and the semiconducting GaAs phase. Another example is Pt-C [39], which are immiscible systems that do not form carbides. The challenge here is that when the carbon bonds are saturated, the chemical interaction between C and Pt is essentially nonbonding, but the potential must nevertheless have local minima for experimentally reported thermodynamically unstable compounds. Recently, Juslin *et al* developed a BOP for the W-C-H system [40]. In this system, the constituents can take on many different phases, e. g. a cubic W phase, which is metallic, and the hexagonal WC phase, which contains both metallic W-W bonds and covalent W-C bonds. The ability to predict relative stabilities between different phases is a test of the versatility of the BOP formalism.

CHAPTER 4

Modeling of interfaces

In reality, the properties of a material are to a large degree determined by the presence of defects. In condensed matter theory, the object of study is often a solid of crystalline form, which is well defined by its Bravais lattice and atomic basis. The response of a perfectly periodical solid to external stimuli such as pressure and electric field is mostly well-understood. However, crystalline materials contain point defects such as vacancies and interstitials, line defects such as dislocations, and planar defects such as interfaces, surfaces, and stacking faults. A big challenge for the material theoretician is to understand how defects on an atomic level influence the macroscopic properties of the material. In this work, focus is on the modeling of interfaces. The abundance of interfaces in polycrystalline materials, such as cemented carbides, clearly motivates a thorough understanding of interfacial structures and energetics.

A fundamental quantity when discussing interface energetics is the interface free energy per unit area γ, which is often referred to as simply the interface energy. γ plays an important role in determining equilibrium shapes and sizes of crystals. It also influences the stability and adhesion of interfaces, and is related to wetting behaviour and microstructural development during sintering. Reliable quantitative values of γ for all interfaces in a system is therefore desirable. The prohibitive difficulties of experimentally measuring interface energies make theoretical calculations a valuable tool. In order to discuss how such calculations are performed, we first need a proper definition of γ, which relates the interface energy to the thermodynamics of the interface.

For a system containing a planar interface of area A dividing two phases, the most convenient definition from our perspective, is [41]

$$\gamma = \frac{1}{A}\left(G - \sum_i \mu_i N_i\right), \tag{4.1}$$

where G is the total Gibbs free energy of the system and μ_i is the chemical potential of constituent i. Since the sum $\sum_i \mu_i N_i$ is the total Gibbs free energy of the separated phases, γ is the excess Gibbs free energy per unit interface area associated with the presence of the interface. In the present Thesis, we concentrate on the contribution to G from the internal energy E. Some comments on possible termperature dependent effects are given in Paper II.

To be able to reach a computationally feasible model of an interface, several simplifications have to be made. A real interface can be sharp or diffuse, planar or non-planar, contain impurities of segregant atoms not present in the respective bulk phases, precipitates, vacancies, dislocations, reconstructions, etc. Incorporation of some of these effects into an atomistic model can be made, but a fully realistic description of an interface remains intractable.

In the appended papers, the problem of modeling an interface between two crystals of differing interatomic distances parallel to the interface is studied, i. e. an interface with a misfit. We assume that the interface is planar and sharp. The two crystals have lattice parameters $a^{(1)}$ and $a^{(2)}$ ($a^{(1)} > a^{(2)}$) in the interface plane. Then we can define the misfit

$$f = \frac{a^{(1)} - a^{(2)}}{\frac{1}{2}\left(a^{(1)} + a^{(2)}\right)}. \tag{4.2}$$

Depending on the value of f, the interfaces are divided into three groups: Coherent, semicoherent and incoherent.

The coherent interface has zero misfit ($f = 0$) and the lattices of the adjoining crystals match perfectly at the interface. In reality, coherent interfaces between dissimilar materials is of course rarely seen, but if the thickness of one of the (or both) phases is finite, the thinner phase can be strained to coherence, as is the case when growing thin films on substrates. A coherent interface can also be the result of introducing stand-off dislocations to accomodate the misfit. In some special cases, coherent interfaces can form between solids of the same constituents but different Bravais lattices, such as fcc-Co and hcp-Co in the $(111)_{\mathrm{fcc}} \parallel (0001)_{\mathrm{hcp}}$ interface.

A semicoherent interface has a small misfit, $0 < f \lesssim 0.2$. By considering a film growing on a substrate, it is apparent that for some thickness, it is energetically favorable to relieve the coherency strain and instead let the misfit be taken up by misfit dislocations. The name misfit dislocation could be misleading, since these dislocations are not defects, but a consequence of the geometry of the interface. If the interaction across the interface is pronounced enough to produce localized misfit dislocations, the interface will be characterized by large regions of good fit between the crystals (the coherent region) and small areas in the vicinity of the misfit dislocations where the atomic structure is distorted.

An incoherent interface is the result of a large misfit $f \gtrsim 0.2$ and/or weak bonding across the interface. As misfit grows, the misfit dislocations will approach each other, and eventually the atomic displacements due to neighboring dislocations will cancel. An incoherent interface can also come from joining two crystals with differing patterns in the interface plane, such as a high-angle grain boundary. Incoherent interfaces do not show the long-range correlation in atomic displacement as semicoherent interfaces do.

The goal of the model presented in the appended papers is to find the interface energy as well as the individual atomic relaxations due to the interface for misfits ranging from zero to the incoherent limit. As a first step, rigid body translations of one crystal relative to the other are considered. The interface energy for a certain translation state $\vec{T}$ with respect to some origin is denoted $\gamma(\vec{T})$. By calculating interface energies for all $\vec{T}$, the so called γ-surface is mapped out. For the coherent interface, where there is a translational symmetry in the interface plane, the γ-surface will be periodic with the cell of all non-equivalent in-plane translations [41]. Note that the γ-surface is actually a three-dimensional object, since it is defined for both in- and out-of-plane translations.

To determine the γ-surface in practice, the interface must be commensurate to fit within a supercell of finite size. An interface is rendered coherent by an artificial compression (expansion) of the corresponding phases which yields a common interface lattice parameter a. $\gamma(\vec{T})$ is then calculated within DFT as

$$\gamma(\vec{T}) = \frac{1}{2A}\left(E(\vec{T}) - \sum_i E_i N_i\right), \tag{4.3}$$

where $E(\vec{T})$ is the energy of the interface system, N_i is the number of constituent i in the interface system, and E_i is the energy per atom i retrieved from a bulk calculation of the respective compressed (expanded) phases. This procedure excludes any direct elastic contributions to the interface energy. A factor of $1/2$ (cf. 4.1) is included to take care of the fact, that in the supercell, two interfaces are present due to periodicity. The choice of a in the interval $a^{(2)} \leq a \leq a^{(1)}$ is somewhat arbitrary and is not critical to the calculated γ-surface. In this work, we have chosen a to minimize the elastic energy of the strained bulk systems.

For a coherent interface, an obvious estimation of the interface energy is the minimum of the γ-surface. For an incoherent interface of infinite dimension, neglecting individual atomic relaxations will reduce the γ-surface to a constant value regardless of the translation. We take this constant value as the mean of the γ-surface of its artificially coherent counterpart. Due to the atomic relaxations in the semicoherent interface, the interface energy will in this case lie somewhere between the coherent and incoherent limits, and the exact value of the interface energy depends also on the energy for creating misfit dislocations. In an interface between two soft materials, misfit dislocations will easily be created and the resulting interface energy should be close to the coherent limit. Making a quantitative determination of the interface energy in the semicoherent interface requires a model of the elastic response of the adjoining crystals, which is the subject of the next section.

4.1 PN modeling of semicoherent interfaces

The original model of Peierls-Nabarro [42, 43] (PN) was derived with the aim of describing the displacement field of a dislocation and the critical shear stress for its motion, motivated by the fact that plastic deformation of crystals is to a large extent caused by motion of dislocations along the glide planes. In the simplest formulation of the PN model, an infinite crystal is divided into two elastic parts by a glide plane of the lattice. An edge dislocation with a Burgers vector $\vec{b}$ is introduced into the dividing plane, e. g. by the insertion of an extra half plane in the upper half space. The displacement just above (below) the glide plane is denoted $u^{(1)}(x)$ ($u^{(2)}(x)$), where x is a coordinate along $\vec{b}$. The dislocation is viewed as a distribution of infinitesimal Burgers vectors [21] of size $-\partial u(x)/\partial x\,\mathrm{d}x$ (the sign corresponds to the definition of Burgers vector in 2.21), where $u(x) = u^{(1)}(x) - u^{(2)}(x)$ is the relative displacement of the two half spaces. The atomic nature of the solid is only apparent in the glide plane, where the relative displacement $u(x)$ gives rise to restoring forces $F(u(x))$ acting on the surface of each half space. The effect of the lattice is reflected in F, which has the same periodicity a_g as the glide plane.

The PN integrodifferential equation is obtained by equating the integrated elastic stresses with the restoring atomic forces in the glide plane, which yields

$$\frac{K_\mathrm{e}}{2\pi}\int_{-\infty}^{\infty}\frac{1}{x-x'}\frac{\partial u(x)}{\partial x} = F(u(x)) \tag{4.4}$$

with the boundary conditions $u(\infty) = -b$ and $u(-\infty) = 0$. K_e is the energy coefficient of the dislocation (see 2.2.2) which determines the elastic response as given by the elastic constants (and therefore the crystal structure) and the direction of the Burgers vector.

In the case where the restoring force is assumed sinusoidal, an analytical solution of 4.4 for $u(x)$ exists, as shown already by Peierls in Ref. [42]. In a more realistic treatment, the restoring force is taken from the derivative of the one-dimensional γ-surface

$$F(u(x)) = -\frac{\partial\gamma(u(x))}{\partial u(x)}, \tag{4.5}$$

as proposed by Christian and Vitek [44].

An important quantity describing the motion of dislocations is the Peierls stress σ_P, which is the minimum stress required to move the dislocation. Although the PN model as described above incorporates a periodic restoring force, the dislocation will move without resistance, since in the continuum description, the energy is independent of the position of the dislocation. This is implied by the notion that if $u(x)$ is a solution to the PN equation 4.4, so is $u(x-\tau)$, where τ is an arbitrary translation of the dislocation. The natural resolution of this issue is to consider a misfit energy $W(\tau)$ given by the sum of the γ-surface evaluated at the atomic positions,

$$W(\tau) = \sum_{n=-\infty}^{\infty} a_g\,\gamma(u(na_g-\tau)). \tag{4.6}$$

$W(\tau)$ has a periodicity of a_g and its amplitude is defined as the Peierls barrier W_P. The Peierls stress is the stress needed to overcome this barrier,

$$\sigma_\mathrm{P} = \max\left(\frac{1}{b}\frac{\mathrm{d}W}{\mathrm{d}u}\right). \tag{4.7}$$

An analytical solution for σ_P in the case of a sinusoidal restoring force has been derived [45].

In the appended papers, we have taken on a PN approach to describe the structure and energetics of misfit dislocations in interfaces. Some differences compared to the PN model arise though, because of the different geometry. As a first example, consider a planar interface, where $\hat{x}$ and $\hat{y}$ are two perpendicular unit vectors in the interface plane and $\hat{z}$ is the interface normal. For simplicity, we will first consider an interface between two dissimilar crystals with misfit only in the $\hat{x}$ direction, which allows to consider the γ-surface at a fixed value of y, since the atoms of the respective bulk phases will not be displaced in this direction. A reduction to one dimension is possible, e. g. by fixing the interphase distance, making γ depend only on x.

The misfit gives rise to an array of misfit edge dislocations with a periodicity given by

$$p = \frac{a^{(1)}a^{(2)}}{a^{(1)} - a^{(2)}}. \tag{4.8}$$

Similarly to the original PN model, we define a relative displacement across the interface, $u(x) = u^{(1)}(x) - u^{(2)}(x)$ imposing the boundary conditions $u(-p/2) = u(p/2) = 0$. The energy due to misfit is however not directly related to the relative displacement, as in the original PN model, but rather to the disregistry $U(x)$ of the atomic planes in the interface. We define

$$U(x) = \frac{a}{2} + \frac{a}{p}x + u(x), \tag{4.9}$$

which gives $U(-p/2) = 0$ and $U(p/2) = a$, where a is the common interface lattice parameter in the coherent interface as previously mentioned. The boundary conditions of $U(x)$ corresponds to one extra atomic plane in the lower crystal.

A basic assumption is that the total interface energy E_{tot} can be decomposed into two terms

$$E_{\mathrm{tot}} = E_{\mathrm{el}} + E_{\mathrm{chem}}, \tag{4.10}$$

where the elastic energy E_{el} results from displacements of atoms, and the chemical energy E_{chem} from the breaking of bonds at the interface. From elasticity theory, it is possible to derive an expression of the elastic energy contained in the two semiinfinite crystals given by

$$E_{\mathrm{el}}\left[u(x)\right] = -\frac{K_{\mathrm{e}}}{4\pi p}\int_{-p/2}^{p/2}\int_{-p/2}^{p/2} \ln\left|\sin\frac{\pi}{p}(x - x')\right| \frac{\partial u(x')}{\partial x}\frac{\partial u(x)}{\partial x}\,\mathrm{d}x'\,\mathrm{d}x, \tag{4.11}$$

where it is worth noting that E_{el} depends only on the relative displacement $u(x)$, which is due to an assumption of continuous stress fields across the interface. The energy coefficient K_{e} depends in a non-trivial way on the elastic constants of both materials in the interface as described in 2.2.2.

The chemical energy is a simple integral of the γ-surface,

$$E_{\mathrm{chem}}\left[u(x)\right] = \frac{1}{p}\int_{-p/2}^{p/2} \gamma\left[U(x)\right]\,\mathrm{d}x. \tag{4.12}$$

The interface energy can now be found by minimizing E_{tot} with respect to the relative displacement $u(x)$. As for the PN model, analytical solutions exist when $\gamma(x)$ is sinusoidal [46, 47].

4.2 Example: The Fe/VN interface

As a first application of the methodology described above, we studied the semicoherent interface between Fe and VN as presented in Paper I. In steels, VN precipitates as small discs of nacl structure within the bcc-Fe grains. An image from an atom probe analysis is given in Figure 4.1. The flat side shows a low misfit of only 2 % with the surrounding Fe matrix, which gives an experimentally well established interface structure of Baker-Nutting relation $(001)_{\mathrm{nacl}} \parallel (001)_{\mathrm{bcc}}, [100]_{\mathrm{nacl}} \parallel [110]_{\mathrm{bcc}}$. As seen in the high resolution electron microscopy (HREM) image in Figure 4.2, the misfit is taken up by misfit dislocations. The side of the disc is incoherent ($f = 44\,\%$) with the matrix. A previous study [48] of the Fe/VN interface neglected the elastic energy, and found a slightly negative ($\sim -0.1\,\mathrm{J/m^2}$) interface energy. The result is physically unreasonable, since it would imply that the respective bulk phases are unstable. This fact motivated the need for a more detailed description of the interface taking semicoherency into account.

The basic input to the calculation is the γ-surface, which we calculated for six high symmetry points in the artificially coherent interface. For these six points, we calculated γ also as a function of intergrain distance z. The Fe/VN interface has a misfit in both directions of the interface, and, as a consequence atoms will relax both in the interface plane, but also perpendicularly due to local Poisson effects and the corrugation of the γ-surface. To allow an analytical solution for the interface energy within the PN model, the dimensionality of the problem must be reduced. To go from 3D to 2D, we remove the z-dependence in the γ-surface by using the optimal intergrain distance at all points, i. e. $\gamma(x,y) = \min_z \gamma(x,y,z)$. To reach the 1D case, we must choose a cut of constant y in the γ-surface. The preferred interfacial site for Fe is on top of N, which suggested us to use a cut between these sites, which is further motivated by the fact that it gives the lowest chemical energy. Furthermore, if the true γ-surface is approximated by a single cosine-function an analytical solution exists.

To extend the 1D interface energy to the physically relevant situation of a 2D dislocation network, we multiply the deviation from the coherent interface by 2, which makes

$$E_{\mathrm{tot,1D}} = 2E_{\mathrm{el}} + 2(E_{\mathrm{chem}} - E_{\mathrm{coh}}) + E_{\mathrm{coh}}, \tag{4.13}$$

where E_{coh} is the energy of the coherent interface. Errors induced by this formula will be significant only in the region where dislocations intersect. For a low misfit interface, the area of this region will be small compared to the total interface area, and hence the approximation is valid in the low misfit limit.

An assessment of the validity of the computational models was performed by comparing the analytical solution with an atomistic model. The Fe phase was de-

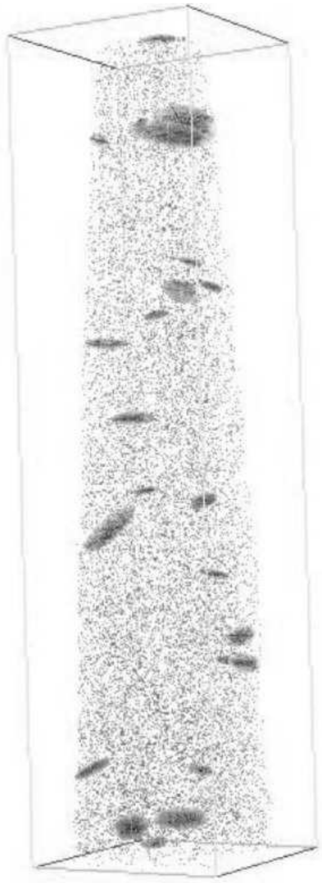

Figure 4.1: An atom probe analysis of steel. VN is seen as discs. The original image is published in [49].

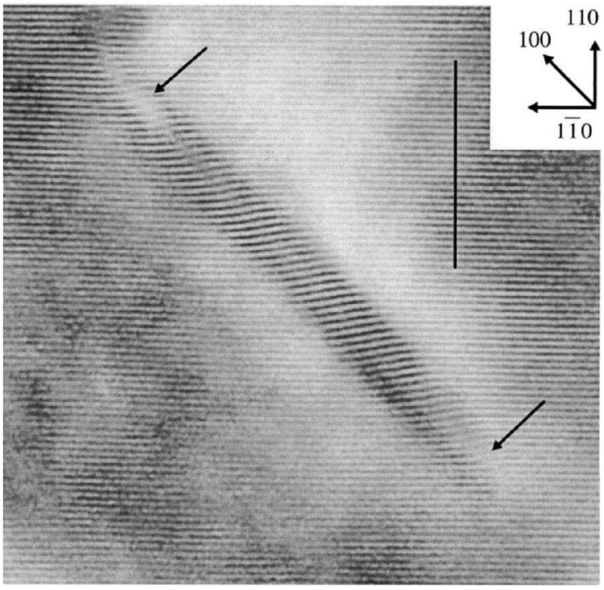

Figure 4.2: An HREM image of the Fe/VN interface from Ref. [50] showing the $(110)_{\mathrm{bcc}}$ and $(111)_{\mathrm{nacl}}$ lattice fringes. Two misfit dislocations are present in the image. Their separation agrees well with the theoretical prediction of $p = 141\,\text{Å}$ (the vertical bar corresponds to $60\,\text{Å}$).

scribed by an EAM potential [33], but since no model potential for VN is available in the literature, we regarded the VN phase as rigid. An atomistic description, where atoms are free to relax, allows an explicit comparison of the effects of going from 3D to 1D and to use a single cosine functon instead of utilizing all information in the γ-surface. For the analytical solutions, we also compared the effect of assuming that the Fe phase is elastically isotropic.

The agreement between all computational models was good and the total interface energy was found to be $\sim 0.5\,\mathrm{J/m^2}$ with differences between the models around $0.01 - 0.05\,\mathrm{J/m^2}$. The largest discrepancy between analytical and atomistic models was found in the case when Fe is assumed to be isotropic, which yields an overestimation of the interface energy of $0.06\,\mathrm{J/m^2}$. To continue, we also made an analytical calculation in the case where both Fe and VN are treated as elastic media with appropriate elastic constants and found an interface energy of $0.32\,\mathrm{J/m^2}$, which is our final estimate of the interface energy.

An important conclusion from the work in paper I is that such small misfit as $2\,\%$ has a large influence on the interface energy. When studying semicoherent interfaces, elastic effects cannot be neglected and our method provides a fast way of assessing the interface energy. In Paper II, the method was applied also to the Fe/ScN and Fe/TiN interfaces.

4.3 Example: Special grain boundaries in cemented carbides

When studying a magnified image (e. g. Figure 1.4) of a sintered cemented carbide, it is apparent that the mechanical properties of the final product is far from being completely described just by the bulk properties of the carbide grains and binder that make up the material. The structure, strength and thermodynamics of interphase and grain boundaries are of great importance for the microstructure. Examples of frequently used quantitative measures of microstructure include composition of the phases, distribution of carbide grain size and the amount of binder between grains.

The distribution of misorientation in grain boundaries has not traditionally been used to quantify a microstructure, because of the tedious experimental work required for determining the orientation of interfacing grains. In the TEM, diffraction patterns in neighboring grains have been used to find the relative orientation. Difficulties in acquiring proper specimens and finding measurable grain boundaries have limited the number of investigated grain boundaries to at most a few tens for a normal study. The introduction of the electron backscatter diffraction technique (EBSD) [51] has made a definite improvement of the experimental situation and now allows experimentalists to investigate thousands of grain boundaries within a couple of hours. Today, EBSD can be used as an important tool for characterizing microstructure. By scanning the surface of a specimen, a computer quickly determines the orientation of grains pixel by pixel by examining the corresponding diffraction pattern.

In order to specify a grain boundary, some geometrical considerations are needed. Let us denote the interfacing grains 1 and 2. The lattices of grain 1 and 2 are thought to be extended over all space. Then lattice 1 is rotated around a common rotation axis (possible followed by a translation) until the lattice sites of 1 and 2 coincide. The angle of rotation around the axis is the misorientation angle. A complete definition of the grain boundary also requires knowledge of the interface planes.

A frequently used parameter to characterize a grain boundary is its Σ value, which is related to the coincident site lattice (CSL) of the boundary [41]. To construct a CSL, the two lattices of grain 1 and 2 are, once again, thought to be extended over all space. Then lattice 1 is translated until one of its sites coincide with a site of lattice 2. The CSL is now the lattice of all coincident sites. The value of Σ is defined as the ratio of the volume of a unit cell of the CSL to the volume of a unit cell of the crystal lattice. An arbitrary grain boundary does not need to have a finite Σ. A low Σ can be an indication of a low-energetic boundary. If we consider stacking faults as a special class of grain boundaries, these would give $\Sigma = 1$ and often a lower energy than the average grain boundary [52].

Since the ratio $c/a = 0.976$ for WC is close to 1, it is possible for WC to form low Σ boundaries in the $c/a = 1$ approximation. Hagège *et al* [53] have characterized several low Σ grain boundaries. The lowest possible in a hexagonal system is $\Sigma = 2$, which is formed by rotating one half of a crystal by 90° around the prismatic $\left[10\bar{1}0\right]$ axis. Note that the $\Sigma = 2$ criterion does not put any constraint on the planes of interface.

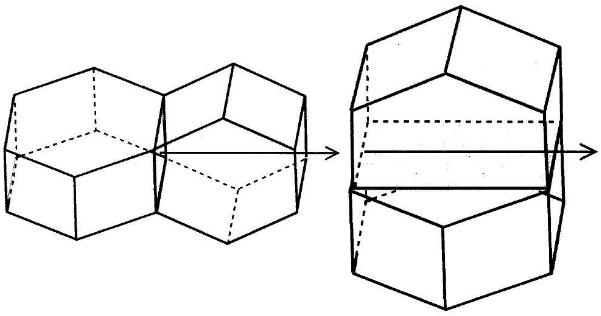

Figure 4.3: Simple sketches of the (left) pure twist and (right) pure tilt $\Sigma = 2$ boundaries. The common rotation axis is the prismatic $\left[10\bar{1}0\right]$ axis.

In an arbitrary grain boundary, there will be no simple relationship between the axis of rotation and the interface plane. However, there are two types of boundaries that are simpler than other: the pure tilt and pure twist boundaries. In a twist boundary, the rotation axis is perpendicular to the interface, and in a tilt boundary the rotation axis lies in the interface. For the rotation of an arbitrary boundary, a decomposition into twist and tilt components is possible. A sketch of the special types of $\Sigma = 2$ boundaries for WC is given in Figure 4.3. Denoting the adjoining crystals 1 and 2, the interface relation for the twist boundary is $\left(10\bar{1}0\right)_1 \parallel \left(10\bar{1}0\right)_2, [0001]_1 \parallel \left[1\bar{2}10\right]_2$ and for the tilt boundary $(0001)_1 \parallel \left(1\bar{2}10\right)_2, \left[10\bar{1}0\right]_1 \parallel \left[10\bar{1}0\right]_2$.

4.3.1 Experimental findings

An example of an image created from EBSD data of a WC-Co specimen is given in Figure 4.4. The gray scale of the image is related to the orientation of the grain. The corresponding misorientation distribution is found in Figure 4.5, where it is plotted together with a random distribution for a microstructure without texture. An outstanding feature of the plot is the distinct peak at 90 °. The plot only gives information about the misorientation angle. A complete description of the misorientation would include also the common rotation axis of the grains. This information can be presented in an axis-angle plot, which for each misorientation angle gives the stereographic projection of the distribution of rotation axes.

The distribution presented in Figure 4.5 is well in line with published experimental work. Kim *et al* [54] performed EBSD studies of a WC-Co material of 6 weight % Co and found two peaks larger than the random distribution. The largest peak corresponding to 11 % of the grain boundaries was found at 90 °. The majority of these grain boundaries had a rotation axis of $\left[10\bar{1}0\right]$ terminated by $\left\{10\bar{1}0\right\}$ planes and are thus $\Sigma = 2$ twist boundaries. In contrast to the distribution in Figure 4.5, they also found a peak corresponding to 3 % of the grain boundaries at 30 °. These were identified with a twist [0001] boundary and an asymmetric [0001] tilt boundary terminated by $\left\{10\bar{1}0\right\}$ and $\left\{1\bar{2}10\right\}$ planes.

The cause of the high frequency of $\Sigma = 2$ boundaries has during recent years

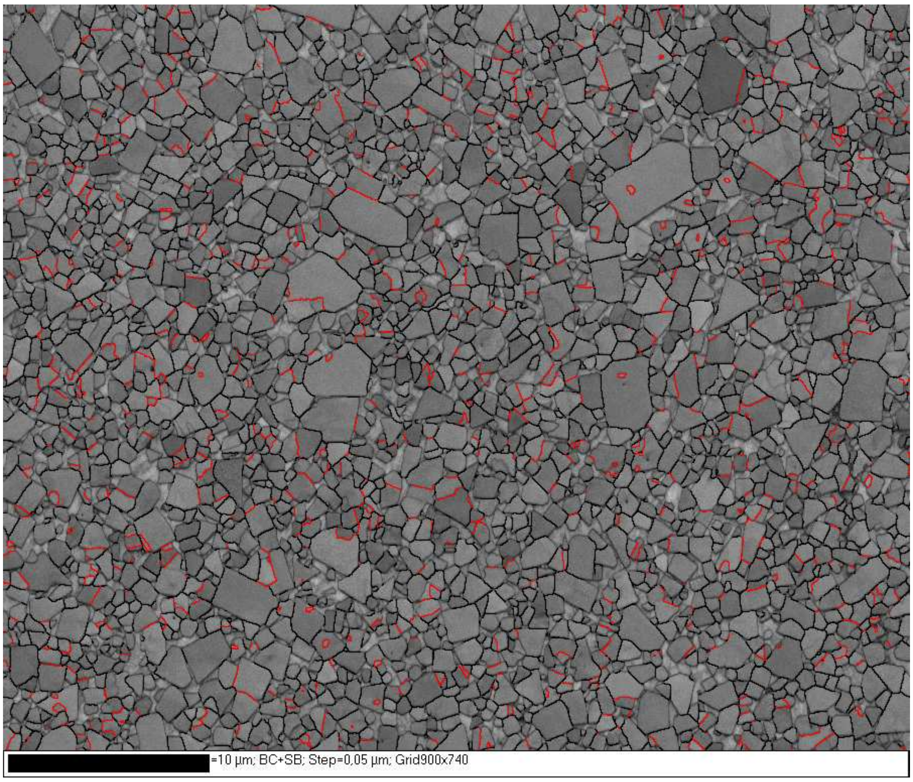

Figure 4.4: An image created from EBSD data of a WC-Co specimen. Black boundaries correspond to a general grain boundary. Boundaries with a misorientation within approximately ±10° from 90° are dark gray. The misorientation makes them candidate $\Sigma = 2$ boundaries. Courtesy of J. Weidow.

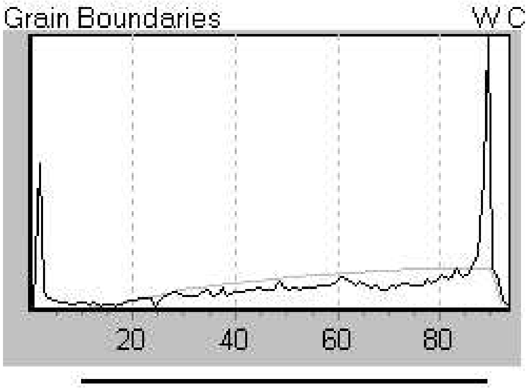

Figure 4.5: A misorientation frequency plot for the specimen in Figure 4.4. The frequency for a random distribution is given in light gray. Courtesy of J. Weidow.

been of both theoretical and experimental interest. Some clues are provided by older experimental work on cobalt segregation to grain boundaries. During sintering of cemented carbides, cobalt will wet carbide surfaces and penetrate grain boundaries. An old controversy in the cemented carbide society was whether a contiguous carbide skeleton exists or if the WC grain boundaries contain a film of segregated cobalt breaking the contiguity. A number of experimental investigations have been conducted to determine the propensity of cobalt segregation to grain boundaries.

Sharma *et al* [55] used STEM equipped with an X-ray detector to measure the atomic Co/W ratio in grain boundaries and in grains. They found that the Co/W ratio was at least three times larger in the grain boundaries, which they interpreted as evidence for the presence of a thin intergranular Co film. Henjered *et al* [56] used atom probe field ion microscopy and analytical TEM and deduced that WC grain boundaries contain Co in a zone of monolayer thickness and that the amount corresponds to about half a monolayer. Using STEM with an X-ray detector, Vicens *et al* [57, 58] found two special grain boundaries of WC that did not show any signs of cobalt segregation. These were the $\Sigma = 2$ twist boundary and a $\Sigma = 5$ twist boundary of the same rotation axis, but with a 53° misorientation angle.

Theoretically, it is known that the $\Sigma = 2$ twist boundary has an exceptionally low grain boundary energy [59], as will be further elucidated later in this Thesis. The low energy interface configuration would provide a strong torque for grains to rotate into the $\Sigma = 2$ relation during the rearrangement stage of the sintering process. The absence of cobalt in some $\Sigma = 2$ boundaries means either that all Co has been squeezed out of the grain boundary during the rearrangement, or that the initial powder contains $\Sigma = 2$ boundaries, into which Co does not diffuse. The latter explaination is more plausible, especially when considering the TEM investigation of WC powder by Lay *et al* [60], which indeed verified the presence of $\Sigma = 2$ boundaries in the powder.

Tungsten carbide powder was also studied by Kim *et al* [61]. They prepared two different WC materials: the first sintered in 40 weight% Cu and the second sintered with 25 weight% Co and small amounts of Mo_2C. The mutual solubility between Cu and WC is negligible causing the grain shape to be conserved during sintering. When sintering in the presence of Mo, the shape of the initial grain will be outlined by a film of precipitated Mo, which makes it possible to distinguish between grain boundaries present in the powder and grain boundaries formed during sintering. By EBSD analysis, they found varying misorientation angles in the WC-Cu material, but with some preference of misorientation angles of 30°, 45°, 75°, and 90°. In the $WC - Mo_2C - Co$ material, the remaining boundaries had misorientation angles of 30°, 72°, and, in particular, approximately 40% were 90° boundaries. Of the 90° boundaries, most were reported to have a common prismatic axis and are therefore $\Sigma = 2$ boundaries.

In a recent study, Kumar *et al* [62] studied the distribution of misorientation angles of grain boundaries as a function of sintering temperature. They too found peaks in the misorientation distribution for angles of 30° and 90°, but, more interestingly, they found that when increasing the sintering temperature from 800°C to

$1400\,^\circ$C the length fraction of $\Sigma = 2$ boundaries decreased from 11 % to 6 %.

4.3.2 Previous calculations

The experimental findings can be compared with the first-principles calculations by Christensen and Wahnström [59, 63], where WC grain boundary energies $\gamma_{\mathrm{WC/WC}}$ and WC/Co interface energies $\gamma_{\mathrm{WC/Co}}$ were calculated. An interesting property, which was studied, is the grain boundary's resistance against Co phase penetration given by the criterion

$$\gamma_{\mathrm{WC/WC}} - 2\gamma_{\mathrm{WC/Co}} > 0. \tag{4.14}$$

The calculations were performed for the $\Sigma = 2$ twist and tilt boundaries and also for a $27\,^\circ$ twist boundary with interfacing prismatic planes. For $\gamma_{\mathrm{WC/Co}}$ two bounds were used. In the lower bound of $\gamma_{\mathrm{WC/Co}}$, the most favorable translation state of Co with respect to WC was used, and in the upper bound a mean of several translation states was used.

All grain boundaries, except the $\Sigma = 2$ twist, fulfilled the phase penetration criterion 4.14. For the $\Sigma = 2$ tilt boundary, also substitutional cobalt segregation in half a monolayer proportion was studied. For certain combinations of translation states and terminations of the boundary, cobalt segregation lowered the WC grain boundary energy, which reduces the expression in 4.14. For a W-terminated (0001)-plane joined with a $\left(1\bar{2}10\right)$-plane, cobalt segregation actually leads to a boundary that *could* be resistant towards Co phase penetration. The uncertainty comes from the determination of $\gamma_{\mathrm{WC/Co}}$. Depending on the chosen bound on $\gamma_{\mathrm{WC/Co}}$, the phase penetration criterion 4.14 is either positive or negative. For no combination of substituted atom (W/C), termination of the (0001)-plane, and translation state a decisive conclusion of resistance against Co penetration could be made.

4.3.3 Current calculations

The calculations presented in [59, 63] rely exclusively on the $c = a$ approximation. The $\Sigma = 2$ twist boundary is known to contain a defect structure in the form of atomic steps as imaged using HREM by several different workers [64, 65, 66]. An example of the defect is given in Figure 4.6.

The defect is a geometrical necessity due to the misfit of the crystals which will increase the grain boundary energy compared with the coherent approximation ($c = a$). To assess this effect, we applied the method developed earlier in this Chapter to the misfit in the $\Sigma = 2$ twist boundary. In order to do this, a detailed model of the geometry is required.

First of all, with $a = 2.906\,\text{Å}$ and $c = 2.837\,\text{Å}$, the periodicity of the interface is given by $p = 119.5\,\text{Å}$, which approximately equals $41a \approx 42c$. Here we propose that each step takes care of half of the misfit on the distance p, so that the steps are separated by an average distance of $p/2 = 59.7\,\text{Å}$, which is the case in the image of Figure 4.6. Also double steps have been reported [64], but these are more seldomly seen and will not be treated here.

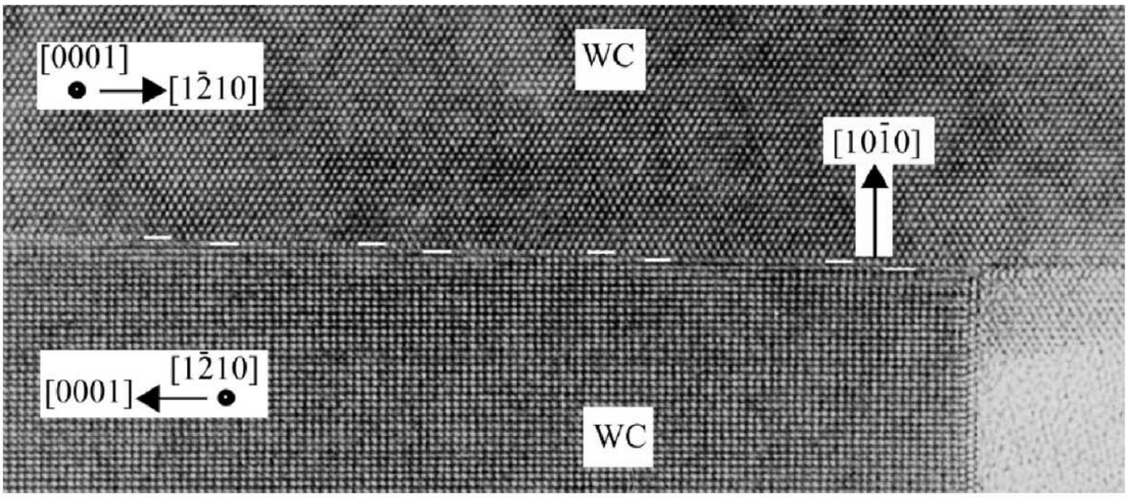

Figure 4.6: A $\Sigma = 2$ twist boundary in cemented carbides from [66]. The steps are marked with white lines. The boundary is imaged using HREM.

The two crystals at the interface can be terminated in three ways: W-W, W-C, or C-C, and we choose to use the W-C termination, since this termination has the largest margin against Co phase penetration. The $\Sigma = 2$ twist boundary contains two non-equivalent choices of dividing planes, as explained in Figure 4.7. We here choose to make a Type I boundary, since it has a lower mean energy.

The γ-surface is interpolated from the data given in [59] and is plotted in Figure 4.8. Apart from a couple of values along the $\left[1\bar{2}13\right]_1$ direction, three different translations states were used for mapping out the γ-surface. The translation state depicted in Figure 4.7 is the minimum energy configuration corresponding to a value of $\gamma = 0.02\,\mathrm{J/m^2}$ and is used as the origin in Figure 4.8. Making a translation $1/6\left[1\bar{2}10\right]_1$ ($1/2\,[0001]_1$) of grain 2 yields $\gamma = 4.67\,\mathrm{J/m^2}$ ($\gamma = 2.82\,\mathrm{J/m^2}$).

Due to symmetry, the γ-surface has two equal minima. This can be understood by studying the sequence of translations in Figure 4.9. In correspondence with the description for making a dislocation in Section 2.2.2, we can imagine making a cut along the interface plane halfway into the boundary. One half of grain 2 is then translated, first with $1/6\left[1\bar{2}10\right]_1$ as in the first drawing of Figure 4.9 and then an additional translation of $1/2\,[0001]_1$. As seen, the resulting translation $1/6\left[1\bar{2}13\right]_1$ brings the interface back to its original translation state, except that the boundary has moved one atomic layer perpendicularly from its original plane. The atomic step in the HREM image of Figure 4.6 can be interpreted as the resulting dislocation of this procedure.

With the misfit dislocation line along $[0001]_1$, we note that the translation $1/6\left[1\bar{2}13\right]_1$ contains both an edge and a screw component. Therefore, the displacement becomes two-valued (u_x and u_y) and the equation for elastic energy 4.11 is generalized to two dimensions. For the case of ordinary dislocations, this has been done previously by

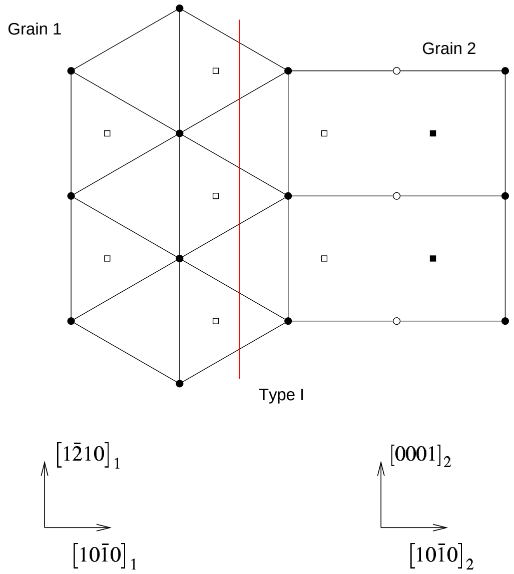

Figure 4.7: The geometry of the $\Sigma = 2$ twist boundary. The gray line marks the dividing plane creating a Type I boundary. By moving the line one atomic step to the right, a Type II boundary is created. Circles or squares denote different atomic species. White or black denotes height (raised or lowered).

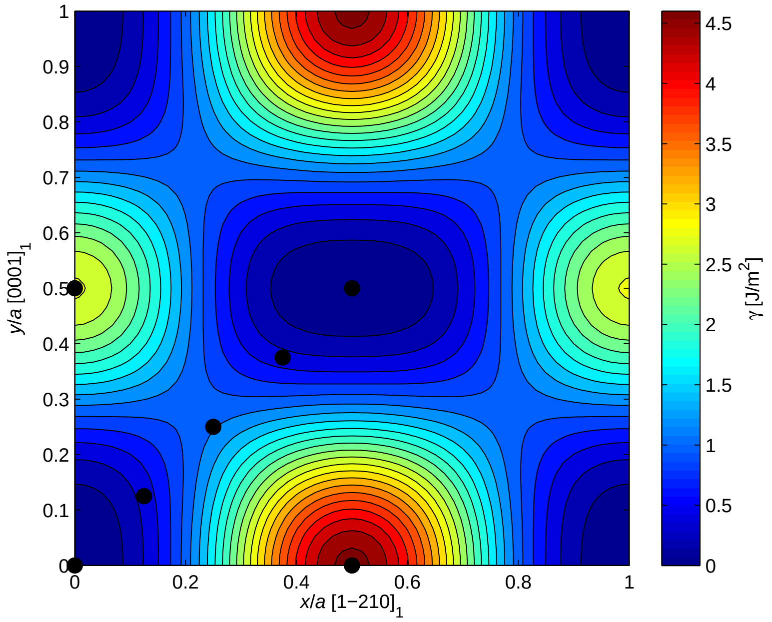

Figure 4.8: The γ-surface of the $\Sigma = 2$ twist boundary. The black dots mark the points used in the interpolation.

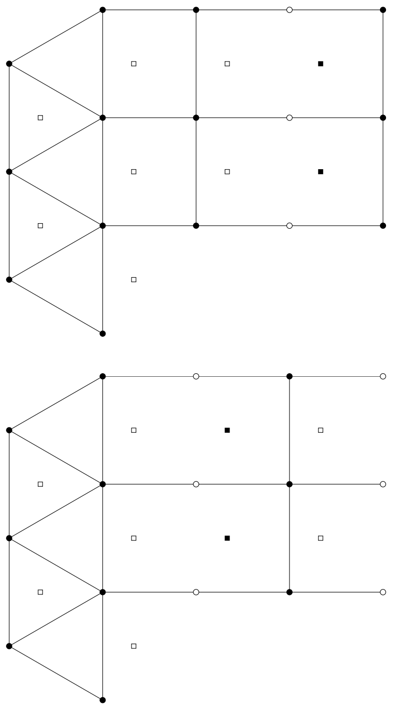

Figure 4.9: Two translations from the original in configuration in Figure 4.7 brings the interface back to its original, except that the boundary plane is moved one atomic plane. The first drawing corresponds to a translation of $1/6\left[1\bar{2}10\right]_1$ and the second to $1/6\left[1\bar{2}13\right]_1$. Circles or squares denote different atomic species. White or black denotes height (raised or lowered).

Schoeck [67, 68], and for the case of misfit dislocations we find

$$\begin{aligned}E_{\mathrm{el}}\left[u_x(x),u_y(x)\right] = -\frac{1}{4\pi p}\int_{-p/2}^{p/2}\int_{-p/2}^{p/2} \ln\left|\sin\frac{\pi}{p}(x-x')\right| \\ \left(K_{\mathrm{e}}\frac{\partial u_x(x')}{\partial x}\frac{\partial u_x(x)}{\partial x}+K_{\mathrm{s}}\frac{\partial u_y(x')}{\partial x}\frac{\partial u_y(x)}{\partial x}\right)\mathrm{d}x'\,\mathrm{d}x,\end{aligned} \tag{4.15}$$

where K_{e} and K_{s} are the energy coefficients for edge and screw dislocations in the interface. Using the elastic constants of WC from [69], we get $K_{\mathrm{e}} = 362\,\mathrm{GPa}$ and $K_{\mathrm{s}} = 300\,\mathrm{GPa}$. The chemical energy changes to

$$E_{\mathrm{chem}}\left[u_x(x),u_y(x)\right] = \frac{1}{p}\int_{-p/2}^{p/2}\gamma\left[U_x(x),U_y(x)\right]\mathrm{d}x, \tag{4.16}$$

where the disregistries $U_x(x)$ and $U_y(x)$ are defined in analogy with 4.9.

The calculations are done for two different geometrical setups as shown in the upper part of Figure 4.10. To the left, the steps are ordered in a repeating up-down sequence, which mimics one of the images given in [64]. To the right, the modeled structure consists of a ladder of steps as imaged in Figure 4.6. The resulting atomic positions projected onto the γ-surface, or rather the resulting disregistry (U_x,U_y) evaluated at the positions of the atoms, are plotted in the lower part of the figure. The resulting grain boundary energies are $0.35\,\mathrm{J/m^2}$ and $0.37\,\mathrm{J/m^2}$, respectively, as compared to $\gamma = 0.02\,\mathrm{J/m^2}$ in the coherent limit. These energies are still very low and can be seen as a minor correction of the coherent approximation. E. g. we have calculated stacking-fault energies on the basal planes which yielded an energy of $0.69\,\mathrm{J/m^2}$. We have also calculated the grain boundary energy when treating the misfit dislocation as a pure edge dislocation, which corresponds to putting the atoms in a straight line on the γ-surface of Figure 4.10. For this case, the energy is $0.52\,\mathrm{J/m^2}$, from which we conclude that the Burgers vector of the step is indeed $1/6\left[1\bar{2}13\right]_1$.

For the $\Sigma = 2$ twist boundary, the result of including the defect has little effect on the resistance towards phase penetration. For the type I boundary, the margin against phase penetration using the data from [59] is $\gamma_{\mathrm{WC/WC}} - 2\gamma_{\mathrm{WC/Co}} = -1.92\,\mathrm{J/m^2}$, which would decrease to about $-1.6\,\mathrm{J/m^2}$ with the present calculation. Still, the $\Sigma = 2$ twist boundary must be regarded as stable.

To our knowledge, a defect structure at the $\Sigma = 2$ tilt boundary has not been imaged. Its grain boundary energy is reported to be $2.1 - 2.6\,\mathrm{J/m^2}$ [63] depending on the C chemical potential (the lower value in the η-limit). Since the defect structure is not known, a rigorous calculation of the effect of the misfit between the a and c parameters on the grain boundary energy cannot be made. However, since the mismatch is the same as in the twist boundary, it is plausible to believe that the correction would be of the same order. The margin against Co phase penetration for the tilt boundary with half a monolayer of segregated Co is somewhere between $0 - 1\,\mathrm{J/m^2}$ depending on termination, substituted atom, and translation state [63]. Adding around $0.4\,\mathrm{J/m^2}$ to the grain boundary energy to account for the misfit decreases this margin, but does not completely eliminate it for all cases.

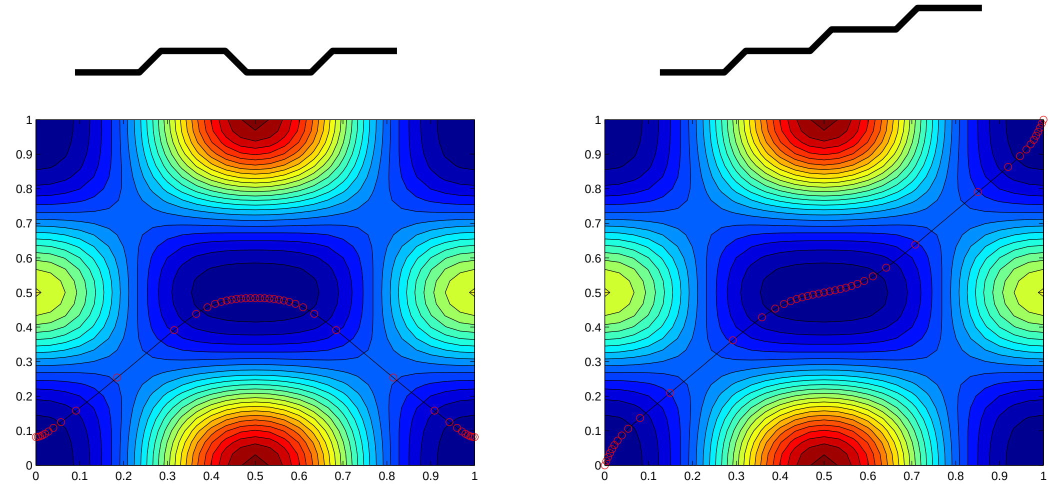

Figure 4.10: Upper part: The modeled structure of steps. Lower part: The circles denote atomic positions in the γ-surface.

The stability of the $\Sigma = 2$ twist boundary is at first sight challenged by the findings of Kumar *et al* [62]. Their study of the length fraction of $\Sigma = 2$ boundaries as function of sintering temperature suggests that $\Sigma = 2$ boundaries are eliminated in greater proportion than other grain boundaries during sintering. However, the authors do not separate the different types of $\Sigma = 2$ boundaries. As the current and previous results show, the driving force for eliminating the grain boundary is one order of magnitude larger for the tilt than the twist boundary. Another interesting result of the Kumar study is the correlation between grain growth and the elimination of $\Sigma = 2$ boundaries. Due to the correlation combined with the short sintering time in the experiment (1 minute), the authors suggest that grain growth in the early stages of sintering occurs not through a dissolution-reprecipitation process, but through grain boundary diffusion.

We have studied one mechanism of diffusion of the $\Sigma = 2$ twist grain boundary involving a movement of the atomic steps. In the most low-energetic state, the steps will be equally separated a distance $21c$ or $20.5a$. Imagining a situation as imaged in Figure 4.6, where the formation of the steps resemble stairs, moving the steps in the same direction would grow one of the adjoining crystals. An intermittent step of this procedure is depicted in Figure 4.11. The energy difference between the state of Figure 4.11 and the most low-energetic is $\Delta E \sim 0.003\,\mathrm{J/m^2}$, making the energy difference for a length L of the step $\Delta E\,pL$. By forming a kink-antikink pair [2], the length L can be reduced. Assuming $L = p/2$ and neglecting the kink formation energy, we get $\left(\Delta E\,p^2/2\right)/k_\mathrm{B}T \sim 10$ where $T = 1500\,\mathrm{K}$ is the temperature and k_B is Boltzmann's constant. Assuming further that the activation energy of moving the step is in the same order, it cannot be ruled out that the steps move by thermal activation. Without explicit atomistic modeling of the boundary motion, no information on the prefactor of such motion can be obtained. However, some information can be drawn from experiments. In an image published in [64], sequential steps are sep-

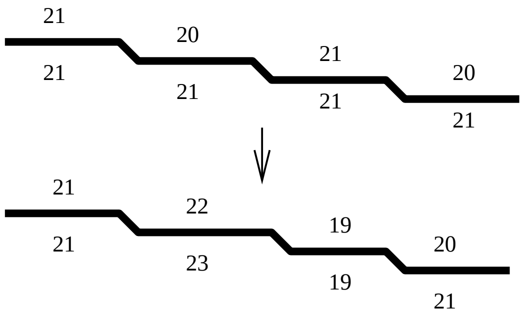

Figure 4.11: A proposed mechanism of grain boundary diffusion in the $\Sigma = 2$ twist boundary. Above the grain boundary, atomic planes are separated a distance a, and below a distance c.

arated by 32 and 9 atomic planes showing that such a state is reachable. Similar processes could be responsible for diffusion of tilt boundaries, where the driving force for elimination is larger. The distance traveled by a single atom in such a transformation is small, tenths of an Ångström maximally.

Near an arbitrary grain boundary, the stoichiometry of W and C may be offset from the ideal. In such case, grain boundary diffusion would require individual atoms to diffuse much longer distances than Ångströms. Co infiltration will probably act as a hinder to grain boundary diffusion, since the low solubility of Co in bulk WC requires that the Co atoms would have to diffuse along with the grain boundary.

To conclude, the defect structure at the $\Sigma = 2$ twist boundary is identified as a step of Burgers vector $1/6\left[1\bar{2}13\right]_1$. Including the effect of the misfit to the grain boundary energy increases its value from $0.02\,\mathrm{J/m^2}$ in the coherent approximation to about $0.35\,\mathrm{J/m^2}$. This correction should have little implication for the twist boundary's resistance against Co phase penetration. We have also proposed a likely mechanism for grain boundary diffusion of $\Sigma = 2$ boundaries, that involves motion of the defect structure due to misfit. Such mechanism should not be possible in a more arbitrary grain boundary or in a grain boundary infiltrated by Co.

CHAPTER 5

Summary and Outlook

The goal of this Thesis has been to obtain a better understanding of interfacial structures and energetics, in particular of semicoherent interfaces. Previous first-principles work in the field has often excluded the effect of misfit. Therefore, we have presented a simple model combining the interfacial interaction from first-principles methods with a continuum description to account for the elastic displacements. The accuracy of the model has been satisfactorily tested against atomistic modelling.

We have investigated the effect of misfit on interfaces in two classes of materials: steels and cemented carbides. In the first case, we studied the Fe/VN interface. The results showed that even a small misfit (2 %) has a large influence on the interface energy. In the second case, we applied the method to the semicoherent $\Sigma = 2$ twist boundary found in both tungsten carbide powder and sintered cemented carbides. The results were discussed in the context of grain boundary evolution during sintering.

As a continuation on the research on cemented carbides, several interesting issues have arisen during our work. It is well-known that additions of V and Cr act as grain growth inhibitors. The exact mechanism is however not known. To some degree, the dopants alter both the solidus-liquidus temperature of the binder and the solubility of W in the melt during sintering thereby affecting the dissolution-reprecipitation process. It is generally accepted [70] that the growth mechanism in WC-Co is controlled by the reaction rates of the dissolution or reprecipitation at the surfaces of the carbide grains and not by the diffusion of W in the liquid phase. Therefore, the answer to the question of grain growth inhibiting mechanism should be sought for at the WC-binder interface.

HREM images of VC-doped WC-Co show the presence of thin films of cubic (V,W)C_x at WC-Co interfaces and between WC grains [71, 66, 72]. The cubic phase has also been seen as small precipitates in pockets between WC grains and binder.

Similar studies have been performed also for Cr-doped WC-Co. Some workers [73] report a thin face-centered cubic layer at the interface between WC and Co, whereas others [74] do not see films at the interfaces but nevertheless a Cr segregation to both WC/Co and WC/WC interfaces. A recent HREM study [75] of WC-Co without dopants also revealed a thin cubic WC_x film in the WC/Co interface. It has been speculated that these films hinder the dissolution-reprecipitation process and/or that they are involved in the growth mechanism of WC. It is, however, not known if the films exist during sintering or if they form during cooling. It is also suspected that they act detrimentally on the adhesion between WC and Co.

A thorough theoretical investigation of the prerequisites for formation of thin films in the WC/Co interface in both doped and undoped material is therefore a good proposal for future work. Such an investigation must take into account both the effect of temperature and composition of the film. To predict the conditions for formation, first-principles calculations must be combined with thermodynamical data of the Gibbs free energy for the bulk phases at hand.

From a modeling perspective, it would be interesting to study the propensity for segregation of grain growth inhibitors to the interface between liquid phase and solid WC using both first-principles and classical molecular dynamics at sintering temperatures. Such a study would aim at understanding the binding of grain growth inhibitors to the WC interface in the environment of a liquid and could provide valuable insights into the growth mechanism of WC grains.

Acknowledgments

First of all, I would like to thank my supervisor Göran Wahnström for being helpful and reliable, and always having time to discuss physical problems. Your ability of keeping focus on the important physics of a problem is admirable. Of course, your relaxed and cool style is highly appreciated.

Past and present members of the Material and Surface Theory group are also acknowledged, especially Mikael Christensen for giving me a good start.

I would like to thank all participants involved in our research project: Hans-Olof Andrén and Jonathan Weidow of the Microscopy and Microanalysis group, Chalmers; Susanne Norgren, Mattias Elfwing, and Per Gustafson of Sandvik Tooling; Sabine Lay, Valérie Bounhoure, and Jean-Michel Missiaen of LTPCM Grenoble; Emmanuel Pauty of Sandvik Hard Materials; and Jenni Zackrisson and Bo Jansson of Seco Tools. The density of cemented carbide knowledge at our project meetings ought to be world-leading. The visits to the companies have been valuable and has put perspective on our research. A special thanks to Bo for the Thermocalc course and for thermodynamical discussions.

Bibliography

[1] R. W. K. Honeycombe and H. K. D. H. Bhadeshia, *Steels - Microstructure and Properties* (Edward Arnold, London, 1995).

[2] J. P. Hirth and J. Lothe, *Theory of Dislocations*, 2 ed. (Wiley, New York, 1982).

[3] K. H. J. Buschow *et al*, *The Encyclopedia of Science: Materials and Technology*, `http://www1.elsevier.com/mrwclus/15/show/Main.htt`, accessed 2007-04-12.

[4] B. Aronsson, *The origins and growth of cemented carbides* (Sandvik Group, Stockholm, 2005).

[5] E. Lassner and W.-D. Schubert, *Tungsten - Properties, Chemistry, Technology of the Element, Alloys, and Chemical Compounds* (Kluwer Academic / Plenum Publishers, New York, 1999).

[6] H.-O. Andrén, *Microstructure of cemented carbides*, Mater. Des. **22**, 491 (2002).

[7] B. Sundman, B. Jansson, and J. O. Andersson, *Thermocalc Databank System*, CALPHAD **9**, 153 (1985).

[8] Y. Wang, M. Heusch, S. Lay, and C. H. Allibert, *Microstructure Evolution in the Cemented Carbides WC-Co - I. Effect of the C/W Ratio on the Morphology and Defects of the WC grains*, Phys. Stat. Sol. (a) **193**, 271 (2002).

[9] H. E. Exner, *Physical and chemical nature of cemented carbides*, Int. Met. Rev. **24**, 149 (1979).

[10] J. Weidow, *Microstructural effects on WC-Co by the addition of V, Cr and Mn*, (Lic. Thesis, Chalmers University of Technology, Göteborg, 2007).

[11] M. Christensen, G. Wahnström, C. Allibert, and S. Lay, *Quantitative Analysis of WC Grain Shape in Sintered WC-Co Cemented Carbides*, Phys. Rev. Lett. **94**, 066105 (2005).

[12] *Crystal Lattice Structures*, `http://cst-www.nrl.navy.mil/lattice/`, accessed 2007-04-19.

[13] J. Willbrand and U. Wieland, *The size of coherent domains in the binder metal of cobalt-bonded tungsten carbide*, Int. J. Powder Met. **8**, 89 (1972).

[14] D. Bacon, D. Barnett, and R. Scattergood, *Anisotropic Continuum Theory of Lattice Defects*, Prog. Mat. Sci. **23**, 51 (1980).

[15] J. O. Kim and J. D. Achenbach, *Elastic constants of single-crystal transition-metal nitride films measured by line-focus acoustic microscopy*, J. Appl. Phys. **72**, 1805 (1992).

[16] J. D. Eshelby, W. T. Read, and W. Shockley, *Anisotropic elasticity with applications to dislocation theory*, Acta Metall. **1**, 251 (1953).

[17] A. N. Stroh, *Dislocations and cracks in anisotropic elasticity*, Philos. Mag. **3**, 625 (1958).

[18] K. Malén and J. Lothe, *Explicit expressions for dislocation derivatives*, Phys. Status Solidi **39**, 287 (1970).

[19] D. M. Barnett and J. Lothe, *Synthesis of the sextic and the integral formalism for dislocations, Greens function and surface waves in anisotropic elastic solids*, Phys. Norv. **7**, 13 (1973).

[20] D. M. Barnett and J. Lothe, *Line force loadings on anisotropic half-spaces and wedges*, Phys. Norv. **8**, 13 (1975).

[21] J. D. Eshelby, *Edge dislocations in anisotropic materials*, Philos. Mag. **40**, 903 (1949).

[22] D. M. Barnett and J. Lothe, *An image force theorem for dislocations in anisotropic bicrystals*, J. Phys.: Metal Phys. **4**, 1618 (1974).

[23] N. W. Ashcroft and N. D. Mermin, *Solid State Physics* (Saunders College Publishing, Fort Worth, 1976).

[24] R. M. Martin, *Electronic Structure - Basic Theory and Practical Methods* (Cambridge University Press, Cambridge, 2004).

[25] P. Hohenberg and W. Kohn, *Inhomogeneous Electron Gas*, Phys. Rev. **136**, B864 (1964).

[26] M. Levy, *Universal Variational Functionals of Electron Densities, First-Order Density Matrices, and Natural Spin-Orbitals and Solution of the v-Representability Problem*, Proc. Natl. Acad. Sci. USA **76**, 6062 (1979).

[27] W. Kohn and L. J. Sham, *Self-Consistent Equations Including Exchange and Correlation Effects*, Phys. Rev. **140**, A1133 (1965).

[28] D. M. Ceperley and B. J. Alder, *Ground State of the Electron Gas by a Stochastic Method*, Phys. Rev. Lett. **45**, 566 (1980).

[29] J. P. Perdew, J. A. Chevary, S. H. Vosko, K. A. Jackson, M. R. Pederson, D. J. Singh, and C. Fiolhais, *Atoms, molecules, solids, and surfaces: Applications of the generalized gradient approximation for exchange and correlation*, Phys. Rev. B **46**, 6671 (1992).

[30] M. W. Finnis and J. E. Sinclair, *A Simple Empirical N-Body Potential for Transition Metals*, Philos. Mag. A **50**, 45 (1984).

[31] J. K. Nørskov and N. D. Lang, *Effective-medium theory of chemical binding: Application to chemisorption*, Phys. Rev. B **21**, 2131 (1980).

[32] M. S. Daw and M. I. Baskes, *Semiempirical, Quantum Mechanical Calculation of Hydrogen Embrittlement in Metals*, Phys. Rev. Lett. **50**, 1285 (1983).

[33] G. Simonelli, R. Pasianot, and E. J. Savino, *Embedded-atom-method interatomic potentials for bcc-iron*, Mat. Res. Soc. Symp. Proc. **291**, 567 (1993).

[34] J. H. Rose, J. R. Smith, F. Guinea, and J. Ferrante, *Universal features of the equation of state of metals*, Phys. Rev. B **29**, 2963 (1984).

[35] F. H. Stillinger and T. A. Weber, *Computer simulation of local order in condensed phases of silicon*, Phys. Rev. B **31**, 5262 (1985).

[36] J. Tersoff, *New empirical approach for the structure and energy of covalent systems*, Phys. Rev. B **37**, 6991 (1988).

[37] D. W. Brenner, *Relationshop between the Embedded-Atom Method and Tersoff Potentials*, Phys. Rev. Lett. **63**, 1022 (1989).

[38] K. Albe, K. Nordlund, J. Nord, and A. Kuronen, *Modeling of compound semiconductors: Analytical bond-order potential for Ga, As, and GaAs*, Phys. Rev. B **66**, 035205 (2002).

[39] K. Albe, K. Nordlund, and R. S. Averback, *Modeling the metal-semiconductor interaction: Analytical bond-order for platinum-carbon*, Phys. Rev. B **65**, 195124 (2002).

[40] N. Juslin, P. Erhart, P. Träskelin, J. Nord, K. O. E. Henriksson, K. Nordlund, E. Salonen, and K. Albe, *Analytical interatomic potential for modeling nonequilibrium processes in the W-C-H system*, J. Appl. Phys. **98**, 123520 (2005).

[41] A. Sutton and R. Balluffi, *Interfaces in Crystalline Materials* (Oxford University Press, Oxford, 1996).

[42] R. E. Peierls, *The size of a dislocation*, Proc. Phys. Soc. **52**, 34 (1940).

[43] F. R. N. Nabarro, *Dislocations in a simple cubic lattice*, Proc. Phys. Soc. **59**, 256 (1947).

[44] J. W. Christian and V. Vitek, *Dislocations and stacking faults*, Rep. Prog. Phys. **33**, 307 (1970).

[45] B. Joós and M. S. Duesbery, *The Peierls Stress of Dislocations: An Analytical Formula*, Phys. Rev. Lett. **78**, 266 (1997).

[46] Y. Yao and T. C. Wang, *The modified Peierls-Nabarro model of interfacial misfit dislocation*, Acta Mater. **47**, 3063 (1999).

[47] Y. Yao, T. Wang, and C. Wang, *Peierls-Nabarro model of interfacial misfit dislocation: An analytic solution*, Phys. Rev. B **59**, 8232 (1999).

[48] J. Hartford, *Interface energy and electron structure for Fe/VN*, Phys. Rev. B **61**, 2221 (2000).

[49] A. Golpayegani, M. Andersson, and H.-O. Andrén, *Microstructure of high boron chromium steel - Part II: Precipitation of nitrides*, Paper VI of A. Golpayegani, *Precipitate stability in creep resistant 9-12 % chromium steels* (Ph. D. Thesis, Chalmers University of Technology, Göteborg, 2006).

[50] T. C. Bor, A. T. W. Kempen, F. D. Tichelaar, E. J. Mittemeijer, and E. van der Geissen, *Diffraction-contrast analysis of misfit strains around inclusions in a matrix: VN particles in* α*-Fe*, Philos. Mag. A **82**, 971 (2002).

[51] F. J. Humphreys, *Review - Grain and subgrain characterisation by electron backscatter diffraction*, J. Mater. Sci. **36**, 3833 (2001).

[52] R. Phillips, *Crystals, defects and microstructures - Modeling across scales* (Cambridge University Press, Cambridge, 2001).

[53] S. Hagège, G. Nouet, and P. Delavignette, *Grain Boundary Analysis in TEM - IV. Coincidence and the Associated Defect Structure in Tungsten Carbide*, Phys. Stat. Sol. (a) **61**, 97 (1980).

[54] C. S. Kim and G. S. Rohrer, *Geometric and Crystallographic Characterization of WC Surfaces and Grain Boundaries in WC-Co Composites*, Interface Sci **12**, 19 (2004).

[55] N. K. Sharma, I. D. Ward, H. L. Fraser, and W. S. Williams, *STEM Analysis of Grain Boundaries in Cemented Carbides*, J. Am. Ceram. Soc. **63**, 194 (1980).

[56] A. Henjered, M. Hellsing, H.-O. Andrén, and H. Nordén, *Quantitative microanalysis of carbide/carbide interfaces in WC-Co-base cemented carbides*, Mater. Sci. Technol. **2**, 847 (1986).

[57] J. Vicens, A. Dubon, J. Y. Laval, M. Benjdir, and G. Nouet, *Cobalt segregation in carbide grain boundaries in WC-Co composites*, J. Physique, Paris **51**, C1 347 (1990).

[58] J. Vicens, M. Benjdir, G. Nouet, A. Dubon, and J. Y. Laval, *Cobalt intergranular segregation in WC-Co composites*, J. Mater. Sci. **29**, 987 (1994).

[59] M. Christensen and G. Wahnström, *Co-phase penetration of $WC(10\bar{1}0)/WC(10\bar{1}0)$ grain boundaries from first principles*, Phys. Rev. B **67**, 115415 (2003).

[60] S. Lay and M. Loubradou, *Characteristics and origin of clusters in submicron WC-Co cermets*, Philos. Mag. A **83**, 2669 (2003).

[61] J.-D. Kim, S.-J. Kang, and J.-W. Lee, *Formation of Grain Boundaries in Liquid-Phase-Sintered WC-Co Alloys*, J. Am. Ceram. Soc. **88**, 500 (2005).

[62] V. Kumar, Z. Z. Fang, S. I. Wright, and M. M. Nowell, *An Analysis of Grain Boundaries and Grain Growth in Cemented Tungsten Carbide Using Orientation Imaging Microscopy*, Metall. Mater. Trans. A **37**, 599 (2006).

[63] M. Christensen and G. Wahnström, *Effects of cobalt intergranular segregation on interface energetics in WC-Co*, Acta Mater. **52**, 2199 (2004).

[64] J. Vicens, E. Laurent-Pinson, J. L. Chermant, and G. Nouet, *Structural analysis and properties of grain boundaries in hexagonal carbides*, J. Physique, Paris **49**, C5 271 (1988).

[65] T. Suzuki, K. Shibuki, T. Suzuki, and Y. Ikuhara, *Grain boundary in cemented carbide*, Philos. Mag. Lett. **71**, 289 (1995).

[66] S. Lay, S. Hamar-Thibault, and A. Lackner, *Location of VC in VC, Cr_3C_2 codoped WC-Co cermets by HREM and EELS*, Int. J. Refract. Met. Hard Mater. **20**, 61 (2002).

[67] G. Schoeck, *The generalized Peierls-Nabarro model*, Philos. Mag. A **69**, 1085 (1994).

[68] G. Schoeck, *The core structure of dislocations. Peierls model vs. atomic simulations in Pd*, Comput. Mater. Sci. **21**, 124 (2001).

[69] M. Lee and R. S. Gilmore, *Single crystal elastic constants of tungsten monocarbide*, J. Mater. Sci **17**, 2657 (1982).

[70] P. Ettmayer, *Hardmetals and Cermets*, Annu. Rev. Mater. Sci. **19**, 145 (1989).

[71] S. Lay, J. Thibault, and S. Hamar-Thibault, *Structure and role of the interfacial layers in VC-rich WC-Co cermets*, Philos. Mag. **83**, 1175 (2003).

[72] S. Lay, S. Hamar-Thibault, and M. Loubradou, *Accomodation of the Lattice Mismatch at the* $VC_x - WC$ *Interface*, Interface Sci. **12**, 187 (2004).

[73] A. Delanoë, M. Bacia, E. Pauty, S. Lay, and C. H. Allibert, *Cr-rich layer at the WC/Co interface in Cr-doped WC-Co cermets: segregation or metastable carbide?*, J. Cryst. Growth **270**, 219 (2004).

[74] T. Yamamoto, Y. Ikuhara, T. Watanabe, T. Sakuma, Y. Taniuchi, K. Okada, and T. Tanase, *High resolution microscopy study in* Cr_3C_2*-doped WC-Co*, J. Mater. Sci. **36**, 3885 (2001).

[75] S. Lay, C. H. Allibert, M. Christensen, and G. Wahnström, *Morphology of WC grains in WC-Co alloys*, in manuscript 2007-01-22.

Paper I

Interface Energy of Semicoherent Metal-Ceramic Interfaces
S. A. E. Johansson, M. Christensen, and G. Wahnström
Physical Review Letters **95**, 226108 (2005)

Paper II

An *ab-initio* based approach for interface energy calculations of semicoherent metal-ceramic interfaces

S. A. E. Johansson, M. Christensen, and G. Wahnström
(in manuscript)